Ore Geology Reviews 157 (2023) 105439

Contents lists available at ScienceDirect

Ore Geology Reviews

journal homepage: www.elsevier.com/locate/oregeorev

Evolution of Fe-Ti oxides within the Tiechagou carbonatite-related iron deposit: Insights from texture and in situ chemical compositions of magnetite and ilmenite

Placide Uwamungu [a], Wei Chen [a,*], Xinfu Zhao [a,b], Kuidong Zhao [a,b], Shaoyong Jiang [a,b]

[a] State Key Laboratory of Geological Processes and Mineral Resources (GPMR), China University of Geosciences, Wuhan 430074, China
[b] Faculty of Earth Resources, China University of Geosciences, Wuhan 430074, China

ARTICLE INFO

Keywords:
Fe-Ti oxide
Magnetite
Ilmenite
Oxy-exsolution
Carbonatite
PCA
Petrogenesis

ABSTRACT

Ilmenite oxy-exsolution in magnetite recording different textures provides information on the Fe-Ti oxide cooling history. Magnetite-ilmenite intergrowths in carbonatites have the potential to offer important insights into the petrogenesis of the hosted ore deposits, whereas they have received limited attention. In this contribution, investigations have been conducted on different types of ilmenite oxy-exsolution hosted by magnetite within the Tiechagou carbonatite-associated iron deposit. Based on textural features, the magmatic magnetite-ilmenite intergrowths have been identified as thin lamellae (Type1), thick lamellae (Type2), fine-grained granular (Type3) and coarse-grained granular oxy-exsolutions (Type4). Major, minor and trace elements of the bulk oxide, magnetite and ilmenite were determined using EMPA and LA-ICP-MS. Bulk MgO and TiO_2 generally decrease from Type1 to Type2 and Type3 to Type4, with Type1 oxides recording the highest. Bulk minor- and trace-element concentrations of all magmatic magnetite-ilmenite varieties exhibit similar trends in continental crust-normalized diagrams. Different magnetite and ilmenite groups are characterized by variable minor and trace element compositions, and have been successfully discriminated using Principal Component Analysis with the most discriminant elements of V, Cr, Ni, Co, Zn, Mn and Mg. Temperature and oxygen fugacity have been determined using WinMIgob, software developed by Yavuz (2021). Textural and chemical features of magnetite and ilmenite in the Tiechagou carbonatite combined with their re-equilibration temperature and oxygen fugacity highlight the evolution history, which is presented into two petrogenetic models. The first model records a significant decrease in temperature from 683 to 338 °C and oxygen fugacity ($logfO_2$) from −14.58 to −34.27, which results in a progressive evolution of ilmenite oxy-exsolution from thin to thick lamellae starting at a supersolvus temperature. The second records a continuing evolution of the magnetite-ilmenite intergrowths from fine-grained to coarse-grained granular oxy-exsolutions through subsolvus oxidation, which is constrained by increase of the average oxygen fugacity ($logfO_2$) from −28.38 to −26.93 at an intermediate temperature of 500–400 °C. Carbon in the oxidized form (e.g., CO_3^{2-}) probably plays a significant role as the oxidizing agent especially when the oxygen fugacity is decreasing and/or low in carbonatite systems.

1. Introduction

The Tiechagou carbonatite in the northernmost part of the Qinling Orogen represents a vital iron ore deposit as it is among few carbonatite-related Fe deposits in this part of Qinling. Magnetite is the most common iron-bearing mineral in this deposit, and also widely recognized as an accessory mineral of carbonatites worldwide (Reguir et al., 2008; Huang et al., 2015; Ivanyuk et al., 2016; Milani et al., 2017). Magmatic magnetite often contains ilmenite and ulvöspinel exsolution lamellae, with the former being the most common form (Buddington and Lindsley, 1964). Magnetite-ulvöspinel forms a complete solid solution at the temperature of 550 °C, and the miscibility gap causes ulvöspinel to exsolve below the solvus (Buddington and Lindsley, 1964; Taylor, 1964; Lilova et al., 2012). Experimental work showed that magnetite-ilmenite intergrowths are not derived from solid solution, and the most accepted theory for the generation of ilmenite exsolutions in magnetite is due to the oxidation of the ulvöspinel, which was proposed by Buddington and Lindsley (1964). During this oxidation-exsolution (oxy-exsolution), an

* Corresponding author.
E-mail address: wchen@cug.edu.cn (W. Chen).

https://doi.org/10.1016/j.oregeorev.2023.105439
Received 18 November 2022; Received in revised form 11 April 2023; Accepted 12 April 2023
Available online 18 April 2023

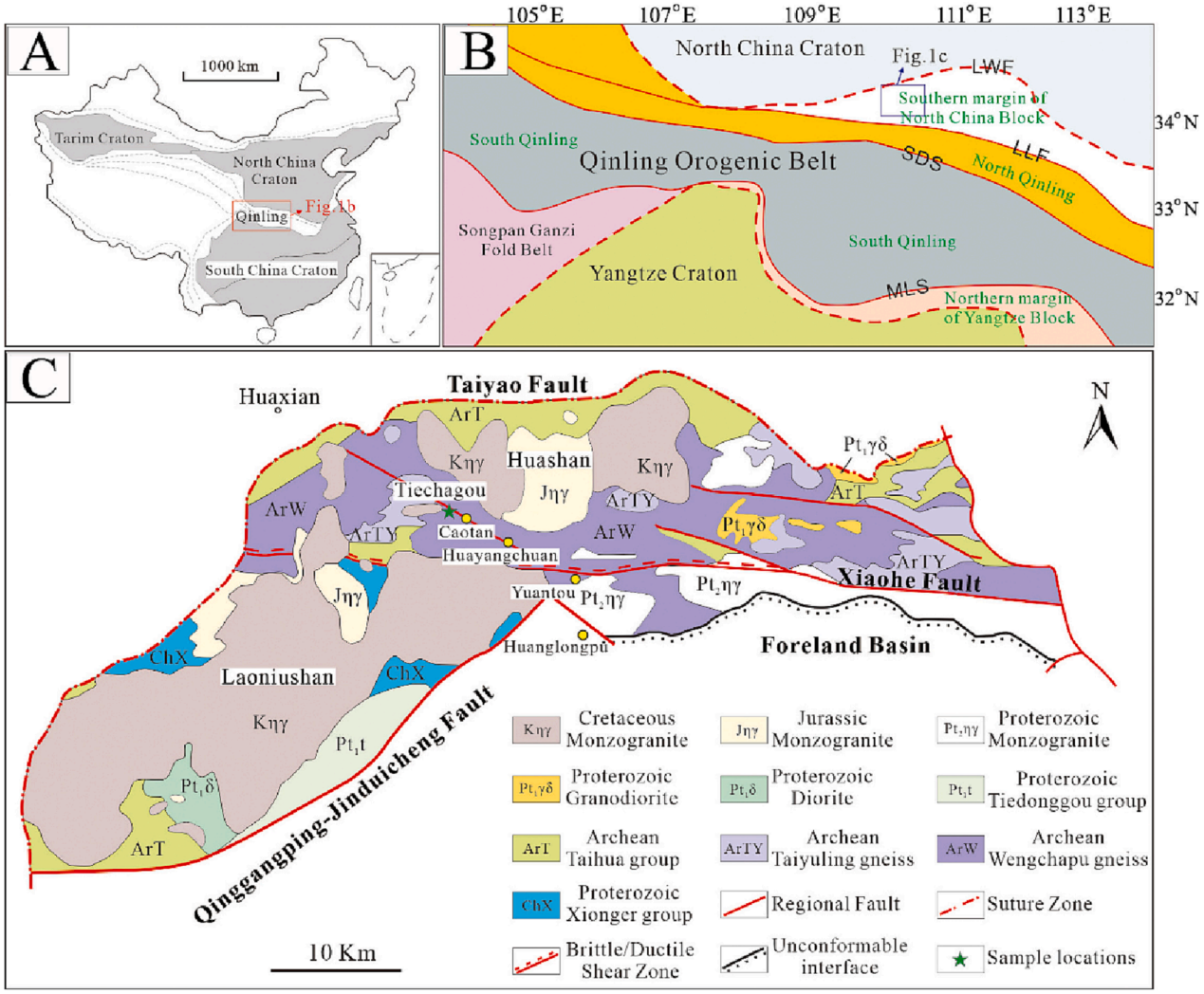

Fig. 1. (A) Geological map of China; (B) regional tectonic map of the Qinling Orogenic Belt; (C) geological map of the Tiechagou district showing the location of the Tiechagou carbonatite. B and C are modified after Zheng et al. (2020). Abbreviations: LLF, Luonan-Luanchuan Fault; LWF, Lingbao-Wuyang Fault; SDS, Shangdan Suture; MLS, Mianlue Suture.

increasing degree of diffusion and oxidation results in a progressive change from (1) a single-phase homogenous spinel, through (2) trellis-type texture of thin ilmenite lamellae in all sets of {111} lattice planes of magnetite, (3) sandwich-type texture of thick ilmenite lamellae principally in one set of {111} planes, (4) internal granular ilmenite exsolutions, to (5) external granular ilmenite exsolutions hosted in magnetite (Buddington and Lindsley, 1964).

Debates are going on for the origin of ilmenite oxy-exsolution in magnetite. Some ascribed it to the subsolvus oxidation of ulvöspinel (Brzozowski et al., 2020; Willemse, 1969), whereas others believe that supersolvus oxidation of ulvöspinel occurs at the origin of ilmenite oxy-exsolution in magnetite (Tan et al., 2016; Wei et al., 2020a, Wei et al., 2020b). In some cases, both sub- and supersolvus (below and above the magnetite-ulvöspinel solvus) processes can generate the oxy-exsolution of ilmenite in magnetite (Von Gruenewaldt et al., 1985; Arguin et al., 2018). Recent experiments confirmed previous observations by Weidner (1982) regarding the importance of carbon in increasing the stability of Ti-poor Fe oxide melts at geologically plausible conditions, which has contributed to the understanding of the origin of some iron ore deposits, such as the El Laco Fe-Ti oxide deposit (Chile; Lindsley and Epler, 2017). The origin of magnetite from carbonatite is also debated, including sedimentary, hydrothermal and magmatic. Huang et al. (2015) concluded that magnetite from the Bayan Obo carbonatite is sedimentary and hydrothermal in nature. Chen et al. (2019) assigned magnetite from different carbonatite deposits to be hydrothermal (Bayan Obo, Hongcheon) and magmatic (Oka, Mushgai Khudag).

A detailed investigation of texture and major-, minor- and trace-element compositions of magnetite from carbonatite is necessary, as it is helpful to decipher the crystallization history of magnetite that provides insights for the genesis of ore deposits (Lee et al., 2005; Ripp et al., 2006; Reguir et al., 2008; Chen et al., 2019). Minor and trace elements, such as Mg, Al, Ti, V, Mn, Co, Ni, Zn and Sn, are mostly concentrated in magnetite, which present a systematic variation (Dare et al., 2014; Nadoll et al., 2014) and can be used to trace the conditions of ore formation including temperature, pressure, cooling rate and oxygen fugacity (Mollo et al., 2013; Canil et al., 2016; Hu et al., 2020). Previous studies showed that minor and trace element compositions of magnetite could also be used to trace the evolution of magma. For instance, it is demonstrated that magnetite crystallized in high-temperature magmatic environments is enriched in a majority of minor and trace elements (including Ti, V, Mn, Mg, Zr, Nb, Hf, Ta and Al) relative to those precipitated from low-temperature fluids (Dare et al., 2014, 2015; Nadoll et al., 2014). In addition, hydrothermal magnetite commonly shows higher concentrations of Ge, Co, Ni, Pb and W compared to their magmatic counterparts (Dare et al., 2014; Nadoll et al., 2014; Huang et al., 2019; Duran et al., 2020). Although the crystal chemistry and

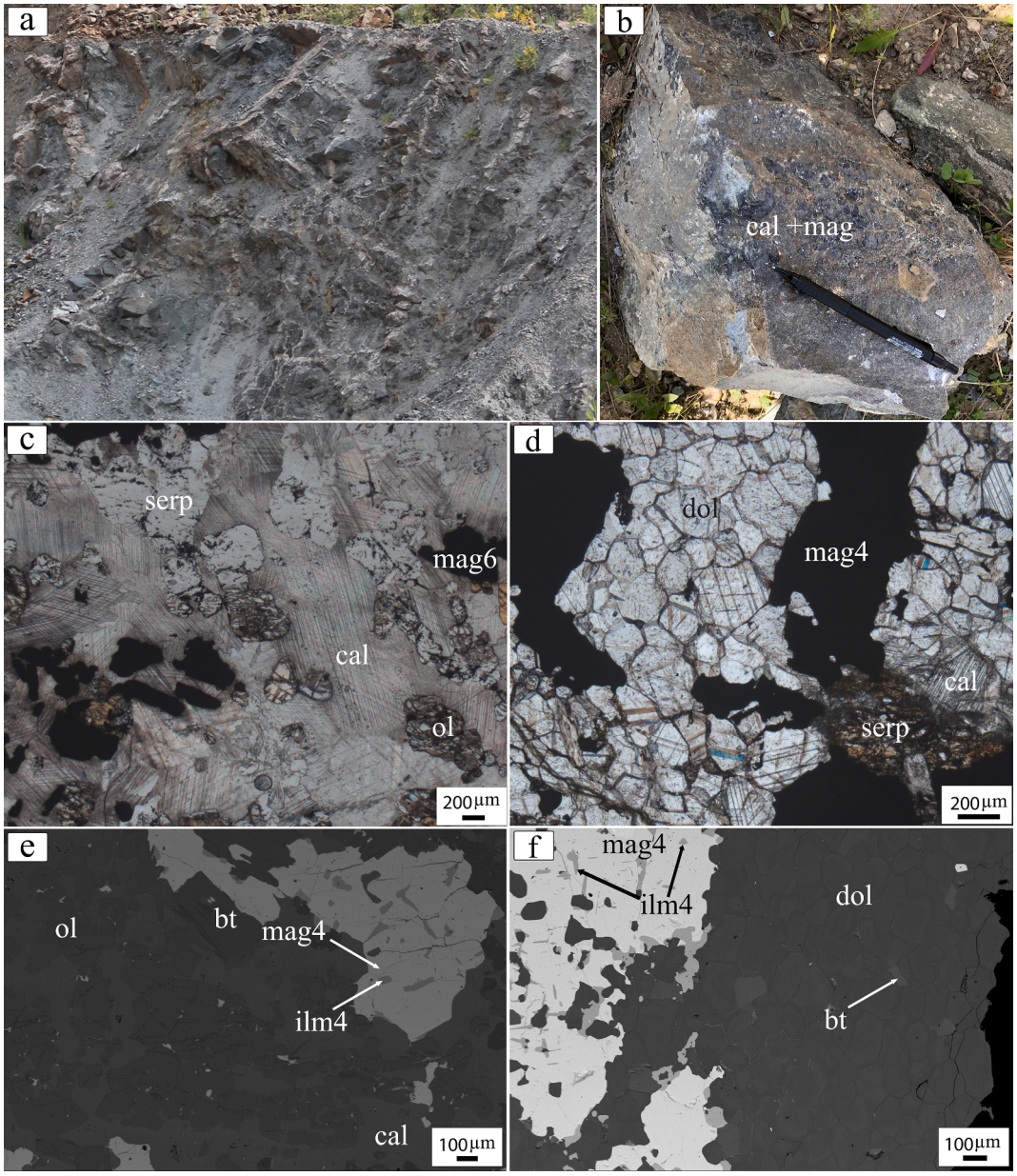

Fig. 2. (A-B) Field observation photos of the Tiechagou carbonatite; (C-F) microphotograph and backscattered electron images showing different minerals within calcio-carbonatite and magnesio-carbonatite. Abbreviations: bt, biotite; cal, calcite; mag, magnetite; ilm, ilmenite; ol, olivine; serp, serpentine.

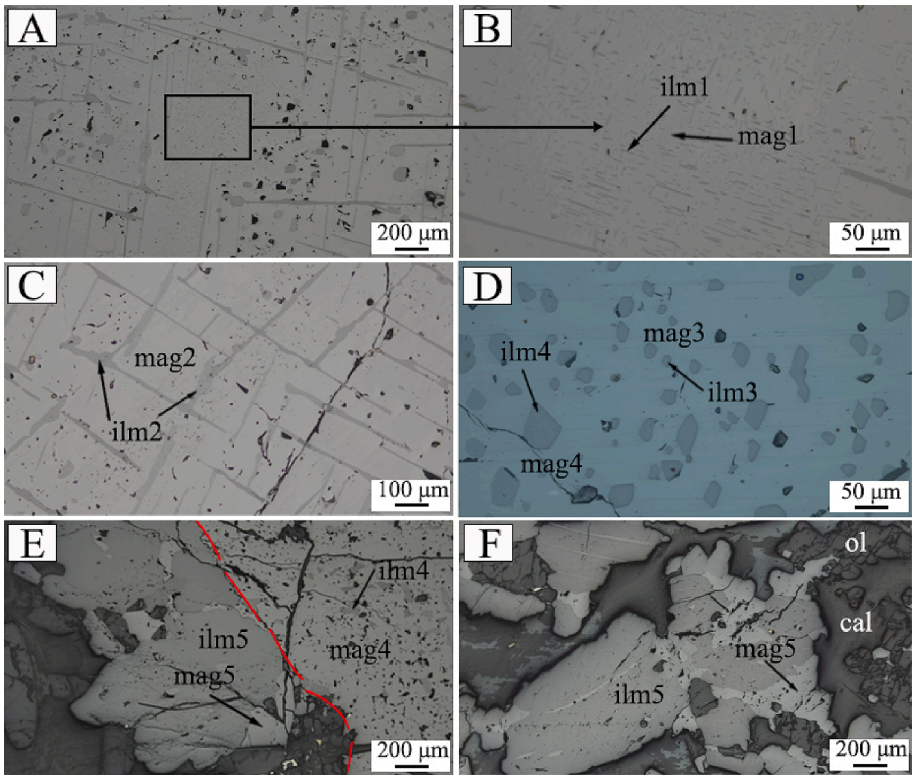

Fig. 3. Reflected light microphotograph outlining different textures of magnetite-ilmenite association within the Tiechagou carbonatite samples. (A) Magnetite hosting thin and thick lamellae and fine-grained granular ilmenite oxy-exsolutions; (B) enlarged image of magnetite that presents thin trellis ilmenite lamellae exsolutions; (C) magnetite that presents thick trellis ilmenite lamellae oxy-exsolutions; (D) magnetite hosting intergrowth of fine- and coarse-grained granular ilmenite oxy-exsolutions; (E) clear boundary between magnetite hosting granular ilmenite oxy-exsolutions and magnetite intergrown with external granular ilmenite; (F) magnetite intergrown with external granular ilmenite. Abbreviations are the same as Fig. 2.

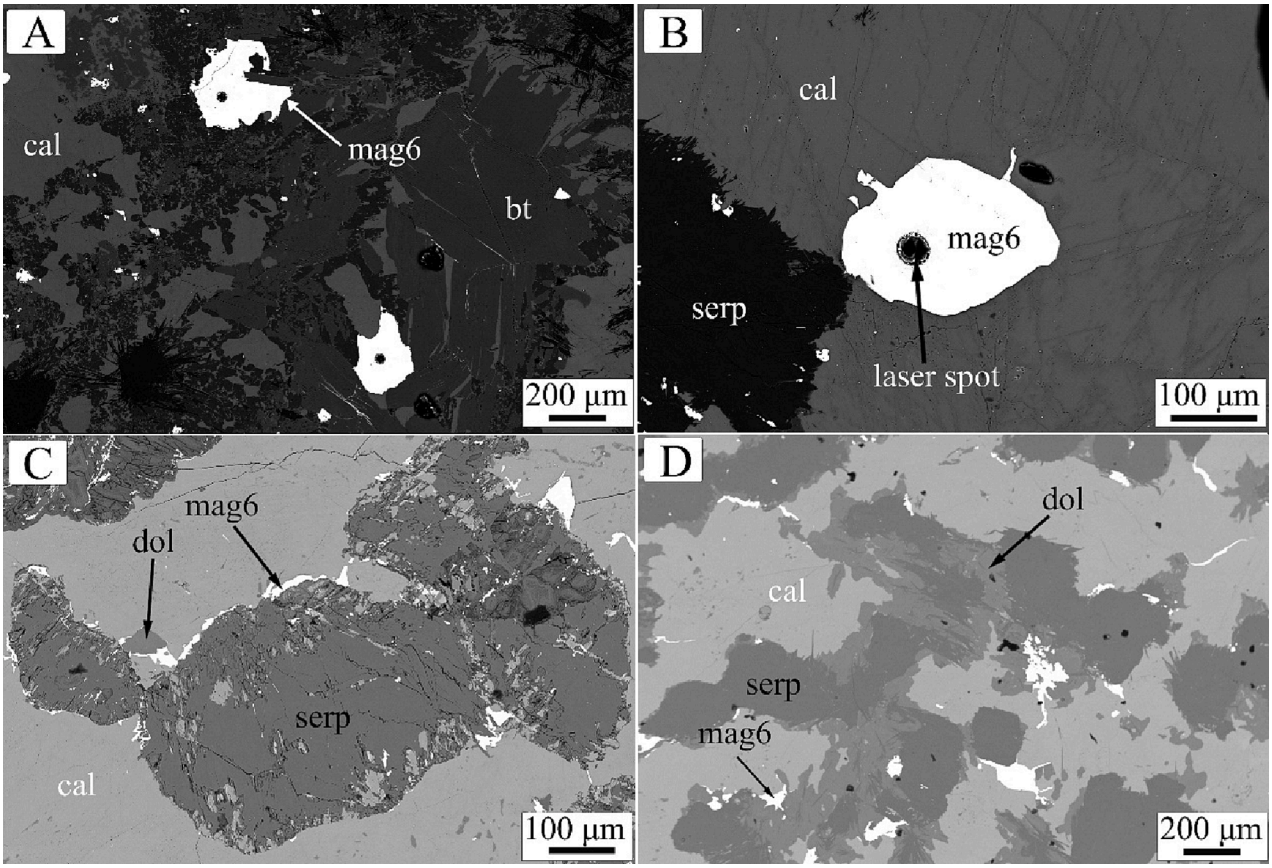

Fig. 4. Backscattered electron images outlining different textures of magnetite within Tiechagou carbonatite samples. (A) Subhedral to anhedral magnetite associated with biotite and serpentine; (B) subhedral magnetite associated with calcite and serpentine; (C-D) anhedral magnetite associated with serpentine and dolomite. Abbreviations are the same as Fig. 2.

thermochemistry of Fe-Ti oxides are complex (Sack, 1982; Ghiorso and Sack, 1991), the chemical compositions are key indicators for their magmatic variability and associated evolution (Haggerty, 1995). Ilmenite is another important Fe-Ti oxide, whereas studies conducted on its minor- and trace-element compositions are relatively limited (Jang and Naslund, 2003; Charlier et al., 2007). A large number of minor and trace elements such as Mn, Mg, V, Cr, Ni, Sc, Nb, Ta, Zr and Hf are hosted by ilmenite as well, which can be used to monitor crystallization and ore-forming processes (Jang and Naslund, 2003; Dare et al., 2012).

In this study, the combined texture and in situ geochemical compositions of different magnetite and ilmenite groups are investigated with the aim to decipher the petrogenesis of Fe-Ti oxides from the Tiechagou carbonatite associated Fe deposit. Our investigation highlights the importance of geothermobarometric approach to decipher the genesis of Fe-Ti oxides from the Tiechagou carbonatite. This study will contribute to the understanding of the formation history of Fe-Ti oxides from carbonatite and other environments.

2. Geological background and sample description

2.1. Geological background

The Qinling Orogenic Belt is one of the most well-known suture zones in eastern Asia and it constitutes a significant part of the Central Orogenic Belt. This orogen comprises four major tectonic units, including the southern margin of the North China Block, North Qinling Orogen, South Qinling Orogen, and the northern margin of the Yangtze Block (Fig. 1A-B). They are separated by three major faults, including the Luonan-Luanchuan, Shangdan and Mianlue faults. The Qinling Orogenic Belt formed by multi-stage collisions between the North China Craton and the Yangtze Craton, and the final Triassic collisional orogeny occurred along the Mianlue suture between 242 and 227 Ma (Wu et al., 2006; Dong and Santosh, 2016). The Tiechagou carbonatite is situated in the southern margin of the North China Block, proximal to the Caotan, Huanglongpu and Huayangchuan carbonatite-associated REE-U-Mo-Pb deposits (Fig. 1C; Bai et al., 2019; Wei et al., 2020a, Wei et al., 2020b; Zheng et al., 2020). The Re–Os isotopic measurements on molybdenite from the Huanglongpu and U–Pb isotopic dating of monazite from Huayangchuan carbonatites gave approximate ages of 220 and 208 Ma, respectively (Stein et al., 1997; Song et al., 2016). The southern margin of the North China Block consists mainly of the Archean Taihua and Paleoproterozoic Xiong'er groups. The Taihua Group (2841–2806 Ma; Kroner et al., 1988) comprises Archaean amphibolite to granulite facies, and the biotite-plagioclase gneiss is the main outcrop sequence at Tiechagou. The Xiong'er Group (1.83–1.74 Ga) comprises weakly metamorphosed andesite, basaltic andesite, dacite and rhyolite, which is overlain by the Meso- to Neoproterozoic Guandaokou and Luanchuan groups (Wang et al., 2019). These Meso- to Neoproterozoic groups are composed of metasedimentary rocks, carbonate and clastic rocks, conglomerate, shale, sandstone, quartzite, phyllite and trachyte (Xu et al., 2011; Jian et al., 2015).

At the Tiechagou carbonatite, two distinct types of carbonatites are observed, which are the calcio-carbonatite and magnesio-carbonatite (Fig. 2A-F). The calcio-carbonatite dominantly consists of calcite, magnetite and olivine with accessory apatite, ilmenite, dolomite, biotite, pyrite, chalcopyrite and humite (Fig. 2B-C, E). The magnesio-carbonatite is dominated by dolomite, with accessory calcite, serpentine, olivine, magnetite, ilmenite, biotite and pyrite (Fig. 2D-F). In both carbonatites, olivine is commonly altered to serpentine. Iron mineralization is characterized by massive magnetite ores that are generally found as layers in the carbonatite body. Magnetite and ilmenite are the most abundant Fe-bearing minerals in the deposit.

2.2. Petrographic characterization of magnetite and ilmenite in the Tiechagou carbonatites

Several texturally distinct varieties of magnetite and ilmenite occur in the Tiechagou carbonatites (Fig. 3). Ilmenite oxy-exsolution in magnetite is a characteristic feature in massive Fe-Ti oxide samples of both calcio- and magnesio-carbonatites. Different varieties of magnetite-ilmenite intergrowth occur at Tiechagou. Magnetite (700 μm to 20 mm) can host thin (1–10 μm) to thick (15–20 μm) trellis ilmenite lamellae (Type1 and Type2, respectively; Fig. 3A-C). Thin trellis lamellae are mostly concentrated in the core of very coarse-grained magnetite (1 to 20 mm), surrounded by thick lamellae (Fig. 3A-C). Magnetite (400–1000 μm) can also host fine-grained (15–20 μm) and coarse-grained (30–50 μm) granular ilmenite oxy-exsolutions (Type3 and Type4, respectively; Fig. 3D-E), which occur together in the same magnetite grain or in different grains (Fig. 3D). Besides, magnetite (30–100 μm) also intergrows with coarse-grained granular ilmenite (40–100 μm) (Type5; Fig. 3E-F). Of note, the boundary is sharp between the magnetite that hosts coarse-grained granular ilmenite oxy-exsolution (Type4) and that intergrows with external ilmenite (Type5; Fig. 3E). Disseminated subhedral and anhedral magnetite grains (Type6) also occur in the Tiechagou calcio-carbonatite samples, associated with serpentine and/or olivine, calcite, dolomite and biotite (Fig. 4A-D). Among these, the subhedral magnetite is coarse-grained (100–200 μm) and commonly associated with biotite and calcite (Fig. 4A-B), whereas the anhedral magnetite is fine-grained (15–20 μm) and closely associated with serpentine and dolomite (Fig. 4C-D).

3. Analytical methods

The investigated Fe-Ti oxide bearing samples have been analysed for their optical properties. Alongside optical microscopy, a scanning electron microscope (SEM) was used to characterize textural features in the Fe-Ti oxides at the State Key Laboratory of Geological Processes and Mineral Resources (GPMR), China University of Geosciences, Wuhan. Back-scattered electron (BSE) images were captured using a high-definition backscattered electron detector connected to a Zeiss Sigma 300 field emission scanning electron microscope.

Major and minor elements in 41 magnetite and associated ilmenite grains identified as different groups were determined using a JEOL JXA-8230 Electron Probe Microanalyzer equipped with five wavelength-dispersive spectrometers (WDS) at the Laboratory of Microscopy and Microanalysis, Wuhan Microbeam Analysis Technology Co., Ltd. The samples were coated with a thin conductive carbon film before analysis. The precautions suggested by Zhang and Yang (2016) were used to minimize the difference of carbon film thickness among samples and obtain an approximately 20 nm coating. Operating conditions for quantitative WDS analyses involve an accelerating voltage of 15 kV, a beam current of 20nA and a spot size of 1 μm. Data were reduced online using a ZAF (atomic number, absorption, fluorescence) correction procedure. The peak counting time was 10 s for Fe and Ti and 20 s for Mg, Mn, Al, Ca, Cr and V. The background counting time was 1/2 of the peak counting time on the high- and low-energy background positions. The peak overlap of Ti Kβ on V Kα and V Kβ on Cr Kα was corrected. The following standards were used for instrument calibration: Pyrope (Al), Diopside (Ca, Mg), Rhodonite (Mn), Rutile (Ti), Hematite (Fe), Chromium (Cr) and Vanadium (V). Major element compositions of the Fe-Ti oxide intergrowth were estimated using combined modal fraction and chemical compositions of magnetite and ilmenite. BSE images were treated based on greyscale difference between ilmenite and magnetite using the segmentation plugin for ImageJ (Sage and Unser, 2003), and the same technique was successfully adopted for the Fe-Ti oxide investigation for the Goldwell complex by Brzozowski et al. (2020). The estimated modal fraction of magnetite and ilmenite based on BSE images was combined with their corresponding average elemental concentration to get the bulk Fe-Ti oxide composition (Table 1).

Table 1
Major element compositions (wt%) of bulk Fe-Ti oxide, magnetite and ilmenite from the Tiechagou carbonatite-related iron deposit.

Sample	bulk Fe-Ti oxide				magnetite											
Type	bulk1	bulk2	bulk3	bulk4	mag1 (n = 17)			mag2 (n = 8)			mag3 (n = 10)			mag4 (n = 5)		
					Min	Max	Average	Min	Max	Average	Min	Max	Average	Min	Max	Average
MgO	4.84	4.53	4.41	4.12	0.69	1.14	0.87	0.88	0.98	0.94	0.75	1.03	0.90	0.76	1.11	1.02
Al_2O_3	0.04	0.04	0.02	0.03	b.d.	0.07	0.05	0.01	0.07	0.05	b.d.	0.04	0.02	0.03	0.05	0.03
CaO	b.d.	b.d.	0.03	b.d.	b.d.	0.09	0.01	b.d.	b.d.	b.d.	b.d.	b.d.	b.d.	b.d.	b.d.	b.d.
TiO_2	14.60	14.03	13.50	12.76	0.36	1.90	0.95	b.d.	0.67	0.13	0.33	1.69	0.81	0.02	1.03	0.27
V_2O_3	0.40	0.45	0.39	0.38	0.34	0.59	0.49	0.45	0.61	0.56	0.43	0.53	0.47	0.42	0.49	0.45
Cr_2O_3	0.02	0.01	0.03	0.03	b.d.	0.04	0.02	b.d.	0.02	0.01	0.01	0.06	0.03	0.02	0.04	0.03
MnO	0.67	0.47	0.70	0.70	b.d.	0.12	0.06	0.02	0.08	0.04	0.05	0.13	0.08	0.05	0.10	0.08
FeO_{total}	74.10	74.62	74.91	76.13	89.80	92.12	90.80	90.30	91.11	90.86	89.88	90.88	90.22	90.44	91.17	90.88
Total	94.65	94.14	93.98	94.15			93.24			92.59			92.53			92.77
$FeO_{cal.}$	n.a	n.a	n.a	n.a	65.27	68.86	66.96	67.50	68.55	68.16	65.43	68.05	66.80	67.01	68.76	68.14
$Fe_2O_{3cal.}$	n.a	n.a	n.a	n.a	29.95	31.46	30.54	29.27	30.01	29.52	29.45	31.28	30.11	29.18	30.87	29.57

Note: b.d. represents below detection.

Minor and trace elements in 89 magnetite, 40 ilmenite and 54 bulk Fe-Ti oxide analyses have been determined using a RESOlution S155-LR 193 nm laser ablation system coupled to a Thermo iCAP-Q Inductively Coupled Plasma Mass Spectrometry (ICP-MS) at GPMR. During this procedure, the following isotopes were analyzed, including ^{7}Li, ^{23}Na, ^{25}Mg, ^{27}Al, ^{29}Si, ^{31}P, ^{39}K, ^{42}Ca, ^{45}Sc, ^{47}Ti, ^{51}V, ^{53}Cr, ^{55}Mn, ^{57}Fe, ^{59}Co, ^{60}Ni, ^{63}Cu, ^{66}Zn, ^{71}Ga, ^{73}Ge, ^{85}Rb, ^{88}Sr, ^{89}Y, ^{90}Zr, ^{93}Nb, ^{95}Mo, ^{115}In, ^{118}Sn, ^{133}Cs, ^{137}Ba, ^{139}La, ^{140}Ce, ^{141}Pr, ^{146}Nd, ^{147}Sm, ^{153}Eu, ^{155}Gd, ^{159}Tb, ^{163}Dy, ^{165}Ho, ^{166}Er, ^{169}Tm, ^{173}Yb, ^{175}Lu, ^{178}Hf, ^{181}Ta, ^{182}W, ^{208}Pb, ^{232}Th and ^{238}U. The ablation of the samples has been achieved utilizing helium as the carrier gas. In a conical ablation cup, helium has been mixed with the argon sample gas. A small amount of nitrogen was added to the central gas flow to increase the sensitivity for most elements by a factor of 2–3 (Hu et al., 2008). Each spot analysis is composed of approximately 30 s of background acquisition and 40 s of sample acquisition. A spot size of 33 μm was used together with a repetition rate of 10 Hz and energy density of 3–5 J cm^{-2}. Raster scanning mode was adopted to determine the bulk concentration of magnetite-ilmenite intergrowth, with a spot size of 33 μm, repetition rate of 10 Hz, energy density of 3 J cm^{-2} and scan speed of 5 μm s^{-1}. Raster is preferable over spot ablation mode for such analysis as the former sampling strategy is more representative. Time-resolved analysis (TRA) spectra for LA-ICP-MS of the magnetite and bulk oxide are shown in the supplementary Fig. 1 and Fig. 2. In this study, the following multiple reference materials have been adopted (NIST612, BIR-1G, BCR-2G, and BHVO-2G) as external standards for concentration determination (Liu et al., 2008). More detailed information for the analytical method can be found in Chen et al. (2019).

4. Results

4.1. Major element compositions of bulk Fe-Ti oxide, ilmenite and magnetite

Major element compositions of the bulk Fe-Ti oxides are in general similar among the different types of magnetite-ilmenite intergrowths, with slight variations observed for TiO_2 showing a decreasing trend from bulk1 to bulk4 (12.76 to 14.60 wt%; Table 1, Fig. 5A). MgO contents (4.12–4.84 wt%) vary less among different types, and a general decreasing trend from bulk1 to bulk4 is also observed. MnO concentration is generally low and shows a narrow range of 0.47–0.70 wt% with the highest observed in bulk3 and bulk4. The bulk concentrations of Al_2O_3 and Cr_2O_3 are both low (below 0.04 wt%). The similarity in the chemical compositions of various types of magnetite hosting ilmenite lamellae (e.g., thin, thick) analyzed together as bulk were also observed by Brzozowski et al. (2020).

Major element compositions of ilmenite show variations mainly in FeO, MnO, MgO and Al_2O_3, which are distinct in different types (Table 1). Thin trellis ilmenite (ilm1) has the highest average MgO concentration of 17.32 wt%, while the coarse-grained granular ilmenite (ilm5) displays the lowest of 13.16 wt%. The highest average MnO content is observed for fine-grained granular ilmenite (ilm3; 2.91 wt%), and the lowest in thick lamellae ilmenite (ilm2; 1.81 wt%). Al_2O_3 content is generally low among all ilmenite types with majority below detection limits. TiO_2 is higher in ilm1, ilm2 and ilm3 (>58 wt%), whereas slightly lower in ilm4 and ilm5 (57.04 and 55.82 wt%). FeO shows an opposite variation trend with higher average contents of 23.84 and 27.47 wt% in ilm4 and ilm5, respectively. Progressive decreases of MgO and MnO with the increase of FeO are observed from thin to thick lamellae and from fine-grained, coarse-grained granular oxy-exsolutions to coarse-grained granular ilmenite, which also correlate with the decrease in TiO_2 of investigated ilmenite (Fig. 5B).

Major element concentrations of magnetite display variations among different groups (mag1, mag2, mag3, mag4, mag5) as shown in Table 1 and Fig. 5C. Magnetite from the Tiechagou carbonatites in general has low TiO_2 contents in the range of below detection limit to 1.90 wt%, which is typical for magnetite from plutonic carbonatites (Gaspar and Wyllie, 1983b; Lee et al., 2005). Among them, magnetite hosting thin ilmenite lamellae (mag1) shows the highest average TiO_2 content of 0.95 wt%. Magnetite hosting fine-grained granular ilmenite oxy-exsolution (mag3) possesses higher TiO_2 (0.81 wt% on average) relative to magnetite hosting coarse-grained granular ilmenite oxy-exsolution (mag4; 0.27 wt%). Magnetite hosting thick ilmenite lamellae (mag2) and magnetite intergrown with coarse-grained granular ilmenite (mag5) are characterized by the lowest TiO_2 (0.13 and 0.14 wt% on average). In general, TiO_2 content decreases from mag1 to mag2 and mag3 to mag4 (Fig. 5C). MgO concentration is generally low in the range of 0.69–1.14 wt%. All magnetite contains low Cr_2O_3 (<0.06 wt%), which is a common feature in magnetite from carbonatites (Bailey and Kearns, 2002; Reguir et al., 2008; Guzmics et al., 2011). Al_2O_3 and MnO are also depleted in the Tiechagou magnetite (<0.13 wt%).

4.2. Minor and trace element compositions of bulk Fe-Ti oxide, ilmenite and magnetite

Minor- and trace-element compositions of ilmenite (ilm1, ilm2 and ilm3) and magnetite (mag1, mag3) were not obtained due to their thin or fine-grained manner (Fig. 3). Minor- and trace-element compositions for ilm4, ilm5 and mag2, mag4, mag5, mag6 and bulks are illustrated in Fig. 6 and presented in Table 2.

Bulk minor- and trace-element concentrations of all magmatic Fe-Ti oxides (bulk1, bulk2, bulk3, and bulk4) show similar behaviors, with positive anomalies of Pb, Hf, Ge, Ta, Nb, Sn, Mn, Ti and V and negative anomalies of Y, Zr, Al, W, Cu, Mo, Ga, Mg, Co and Cr in the continental crust normalized spider diagram (Fig. 6A; Rudnick and Gao, 2003). Overall, bulk Fe-Ti oxide compositions in the Tiechagou carbonatite

			ilmenite															
mag5 (n = 2)			ilm1 (n = 17)			ilm2 (n = 8)			ilm3 (n = 10)			ilm4 (n = 5)			ilm5 (n = 2)		
Min	Max	Average	Min	Max	Average	Min	Max	Average	Min	Max	Average	Min	Max	Average	Min	Max	Average
0.70	0.83	0.77	14.08	19.66	17.32	14.85	16.81	15.90	16.04	18.39	16.86	13.82	15.98	15.14	12.99	13.34	13.16
b.d.	b.d.	b.d.	b.d.	0.26	0.02	b.d.	b.d.	b.d.	b.d.	0.01	b.d.	b.d.	0.01	b.d.	b.d.	b.d.	b.d.
b.d.	b.d.	b.d.	b.d.	b.d.	b.d.	b.d.	b.d.	b.d.	b.d.	1.51	0.15	b.d.	0.05	0.01	b.d.	b.d.	b.d.
0.09	0.18	0.14	51.66	60.08	58.07	57.57	58.55	58.03	57.81	59.12	58.48	55.47	57.60	57.04	55.54	56.09	55.82
0.50	0.52	0.51	0.04	0.17	0.10	0.06	0.15	0.11	0.01	0.14	0.10	0.08	0.16	0.13	0.15	0.15	0.15
0.02	0.03	0.02	b.d.	0.05	0.02	b.d.	0.02	0.01	b.d.	0.05	0.02	b.d.	0.04	0.01	b.d.	0.01	0.01
0.01	0.04	0.03	1.67	4.17	2.54	1.59	2.05	1.81	2.69	3.13	2.91	2.67	3.17	2.88	1.76	1.90	1.83
91.20	91.63	91.41	17.19	28.04	21.27	21.94	24.31	23.20	18.65	22.20	20.62	22.17	26.89	23.84	27.21	27.75	27.48
		92.88			99.34			99.06			99.14			99.06			98.44
68.09	68.65	68.37	0.73	15.24	2.66	0.95	1.80	1.30	b.d	2.44	1.32	1.92	4.81	2.71	2.00	3.72	2.86
29.85	29.93	29.89	14.32	23.90	18.88	20.61	23.46	22.02	17.03	21.73	19.43	19.89	22.60	21.40	24.40	25.41	24.90

have a similar trend with the Oka magnetite whereas more distinct compared to those in the Fe-Ti-V deposit (Fig. 6A; Dare et al., 2014; Chen et al., 2019). Bulk Fe-Ti oxide compositions in the Tiechagou carbonatite is characterized by low concentrations in Al, Ga, V and Cr relative to Fe-Ti-V deposit. Enrichments in Pb, Ta, Nb, Sn, Mn and Mg are observed for bulk Fe-Ti oxide compositions in the Tiechagou carbonatite relative to Fe-Ti-V deposit (Fig. 6A). The distinctive Pb enrichment is common for carbonatites (e.g., Huayangchuan, Huanglongpu) along the southern margin of the North China Block, and Huayangchuan is reported as a U-Pb-polymetallic deposit (Zheng et al., 2020). Of note, the similarities in bulk trace-element concentrations from different types of ilmenite and magnetite intergrowth indicate that these minerals crystallized from a common parental ulvöspinel-magnetite assemblage (Brzozowski et al., 2020).

Ilm4 and ilm5 have Mg and Mn up to thousands of ppm and Nb, Zn and V up to hundreds of ppm (Table 2). Tiechagou ilmenite show positive anomalies of Hf, Ta, Nb, Sn, Mn and Ti and negative anomalies of Al, Ga, Mg and Cr in the continental crust normalized spider diagram (Fig. 6B). Of note, distinct positive anomalies of Hf, Ta, Nb, Mn and Ti observed for the bulk oxides in the continental crust normalized diagram are mostly due to the contribution of ilmenite (Fig. 6A). Ilm4 is more enriched in Ca and Cu relative to ilm5, whereas ilm5 shows higher W, Ta and Nb contents. The exceptionally high concentrations of Ta and Nb in ilm5 are typical for granular ilmenite (Gaspar and Wyllie, 1983a; Jang and Naslund, 2003; Lee et al., 2005).

Minor- and trace-elements in magnetite in the Tiechagou carbonatite generally present similar trends with slight differences in the continental crust normalized spider diagram, displaying negative anomalies of Y, Zr, Ti and Cr and positive anomalies of Pb, Ge and V (Fig. 6B). In general, Tiechagou magnetite contains Mg and V up to thousands, Ti, Mn, Al, Ni, Cr and Zn up to hundreds and Ga, Sn, Cu, Nb, Ta, Sc and Ge below hundreds of ppm. The concentrations of Ge and Ti are almost the same in mag2, mag4 and mag5 whereas the rest vary among different magnetite groups (Fig. 6B; Table 2).

4.3. Fe-Ti oxide geochemical signature investigated by Principal component analysis (PCA)

Principal component analysis (PCA) is a powerful statistical technique used to emphasize variation and bring out strong patterns in a dataset. It is involved in making data easy for better exploration and visualization. PCA is used in our study to enhance the role of different geochemical signals that can help identify various magnetite generations. PCA has been used in many studies to show magnetite compositions and different element associations; recent examples include Makvandi et al. (2016) and Verdugo-Ihl et al. (2021). The following trace elements (Cr, Ni, V, Co, Zn, Ti, Mg, Mn, Ga and Al) of magnetite with concentrations > 10 ppm have been used for PCA in this study. The loading plot of all magnetite groups investigated suggests that Ti and Ga, V and Al, and Mg and Zn are highly correlated (Fig. 7A). The most positive contributors to PC1 are V, Ga and Al with Mn and Co as the negative contributors, whereas Zn, Mg and Mn are the dominant positive contributors to PC2 (Fig. 7A, D). Mag4 and mag5 are not well separated in Fig. 7D, which confirm the magmatic nature for mag5. Magmatic magnetite (mag2, mag4 and mag5) were further investigated, and the loading and score plots display 76.07% of PC1 and 11.46% of PC2 (Fig. 7B, E). Co, V and Zn are the positive contributors to PC1, while Cr is the negative contributor. On the other hand, Cr, Mn and Al are the dominant positive contributors to PC2, whereas Ni and Ga more negatively contribute to PC2 (Fig. 7B). Thus, all different magnetite groups are well discriminated using PCA (Fig. 7D-E).

PCA has also been used for ilmenite groups. Ilmenite loading and score plots display 41.63% of PC1 and 31.52% of PC2 (Fig. 7C, F). Different geochemical signals are observed, V positively correlates with Cr; Ni and Al are highly correlated and negatively correlated to Ti. Nb and Ta are highly correlated, which are negatively correlated to Mg, Mn and Co. The dominant positive contributors to PC1 are V, Cr and Ta, while its negative contributors are Mg and Mn. The main positive contributors to PC2 are Ni, Co and V, whereas Ti, Nb and Ta negatively contribute to PC2 (Fig. 7C). Similar to magnetite, PCA clearly distinguishes the two ilmenite groups based on their chemical compositions (Fig. 7F).

5. Discussion

5.1. Geochemical discrimination of magnetite

The obtained PCA results show that Ti is less efficient compared to V and Ga as discriminating indicators due to its low concentration in Tiechagou magmatic magnetite caused by fractional crystallization of ilmenite (Fig. 7). By comparing our magnetite geochemical data to those from carbonatite worldwide, we inferred that mag2 and mag4 are aligned well with the Phalaborwa magmatic magnetite, while Bayan Obo and Hongcheon hydrothermal magnetite are similar with mag5 and mag6 (Fig. 8; Milani et al., 2017; Chen et al., 2019). These geochemical data are consistent with the textural observation that mag2 and mag4 form as magmatic magnetite, whereas mag5 and mag6 is late magmatic to hydrothermal generations. Both the PCA and Al + Mn vs. Ti + V binary diagrams are proved to be effective discriminant plots to identify different magnetite groups within carbonatites (Figs. 7 and 8). Of note, the magmatic generations of Fe-Ti oxides are dominantly associated with magnesio-carbonatite (e.g., mag4), whereas the more evolved

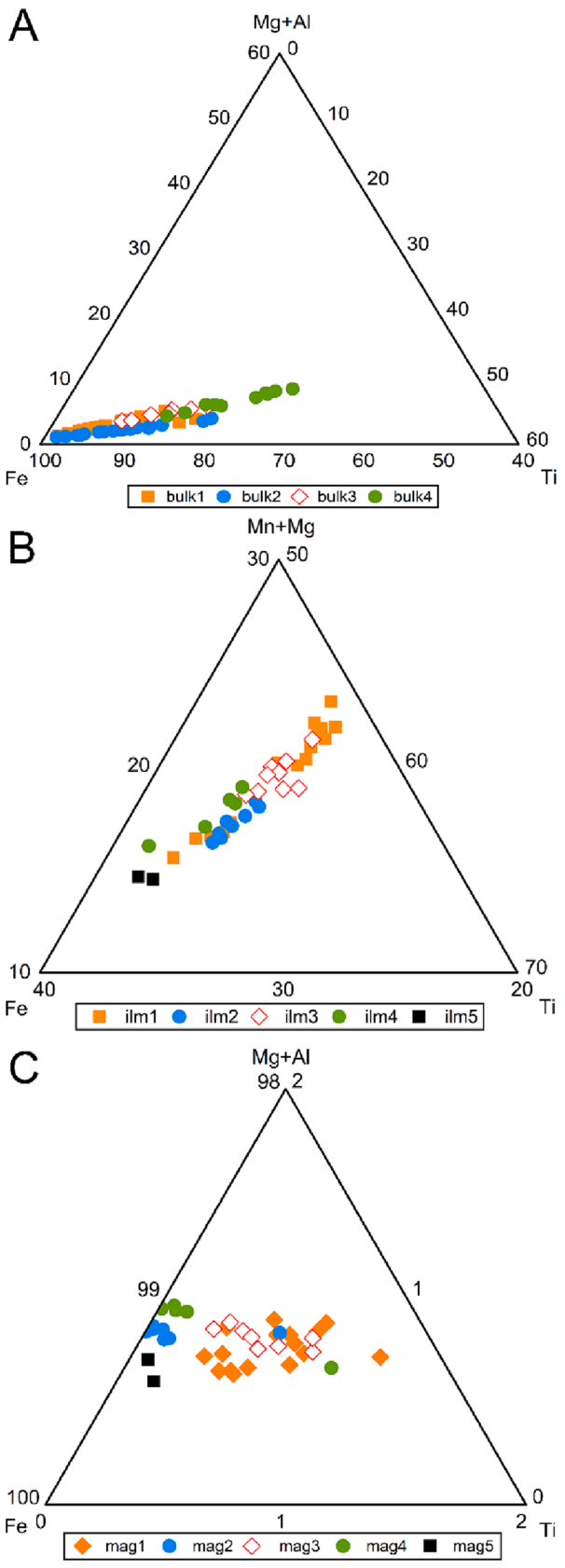

Fig. 5. Ternary diagram illustrating the chemical variation of different types of bulk Fe-Ti oxide (A), ilmenite (B) and magnetite (C).

hydrothermal generations are found only in calcio-carbonatite (mag5 and mag6). This possibly implies that the evolution of Fe-Ti oxides may go hand in hand with the magma evolution from magnesio- to calcio-carbonatites. A similar carbonatite evolution from ferroan through magnesian to calcic compositions was proposed for Bayan Obo by Yang et al. (2019).

5.2. *Temperature and oxygen fugacity as controlling parameters for Fe-Ti oxide crystallization*

The formation of different types of ilmenite and magnetite intergrowth is temperature-dependent. A well-known diagram of Al + Mn vs. Ti + V used to express magnetite formation with the decrease of temperature was modified by Nadoll et al. (2014) after Dupuis and Beaudoin (2011), which also works for the discrimination of magnetite forming in different environments. The drop in temperature among different magmatic magnetite (mag2 to mag4) is well defined (Fig. 8).

Buddington and Lindsley (1964) showed that Fe-Ti oxides could provide important paragenetic information on the rocks containing them and can serve as a useful geological thermometer and oxygen barometer. We used our newly obtained EPMA data for associated magnetite and ilmenite pairs, to calculate the temperature and oxygen fugacity using WinMIgob. It is a program developed by Yavuz (2021) on the basis of the ILMAT sheet of Lepage (2003) with additional magnetite-ilmenite geothermometers and oxygen barometers from Sauerzapf et al. (2008). The uncertainty in temperature is 40–80 °C and 0.5–1 log units of fO_2 as outlined by Spencer and Lindsley (1981). The results show the highest re-equilibration temperature (405–683 °C) and oxygen fugacity ($logfO_2$ = -34.01 to −14.58) in Type1 Fe-Ti oxide intergrowth, implying their earliest formation. Type2 has relatively low temperature (338–464 °C) and oxygen fugacity ($logfO_2$ = -34.27 to −27.92) compared to Type1. Correlated decrease of temperature and oxygen fugacity are observed within Type1 and continued to Type2 (Fig. 9). Granular generations (Type3 and Type4) are characterized by relatively narrow variations in temperature (384–514 °C) but variable oxygen fugacities ($logfO_2$ = −31.45 to −24.31). It is important to highlight that the formation of fine-grained (Type3) to coarse-grained granular (Type4) Fe-Ti oxide intergrowth is dominantly controlled by the increase of the average $logfO_2$ values from −28.38 to −26.93. The observed petrogenetic evolution among different Fe-Ti oxide groups indicated by the re-equilibration temperature and oxygen fugacity is consistent with the observed trend of their textural and elemental features outlined above (Fig. 3, 5B-C). Moreover, the thermo-oxybarometric data (Type1 and Type3) is in good agreement with that of the Fe-Ti oxide from the Phalaborwa carbonatite (Fig. 9; Milani et al., 2017).

5.3. *Associated ilmenite and magnetite evolution history*

It is noteworthy that magnetite with ilmenite lamellae has been previously recognized as magmatic in origin (Ray and Webster, 2007; Reguir et al., 2008; Tan et al., 2016; Milani et al., 2017). Ilmenite lamellae in magnetite are generated by the process of oxy-exsolution and proposed to form at the subsolvus (Willemse, 1969; Von Gruenewaldt et al., 1985; Brzozowski et al., 2020) or supersolvus temperature (Buddington and Lindsley, 1964; Von Gruenewaldt et al., 1985; Tan et al., 2016; Arguin et al., 2018) of the magnetite-ulvöspinel solid solution. In the Tiechagou carbonatite, the oxy-exsolution process occurred both above and below the solvus temperature (550 °C), which is indicated by the best estimated onset temperatures of 683 °C in magnetite hosting thin ilmenite lamellae (Type1) and 514 °C in magnetite hosting fine-grained granular ilmenite (Type3) as shown in Fig. 10, respectively. Of note, the original titanomagnetite temperature (bulk1 to bulk4) has also been estimated adopting the $T_{Mg\text{-}mag}$ (=-8344 (±322)/[lnX_{Mg} − 4.13(±0.28)]-273) geothermometer established by Canil and Lacourse (2020), which considers an uncertainty of ± 50 °C.

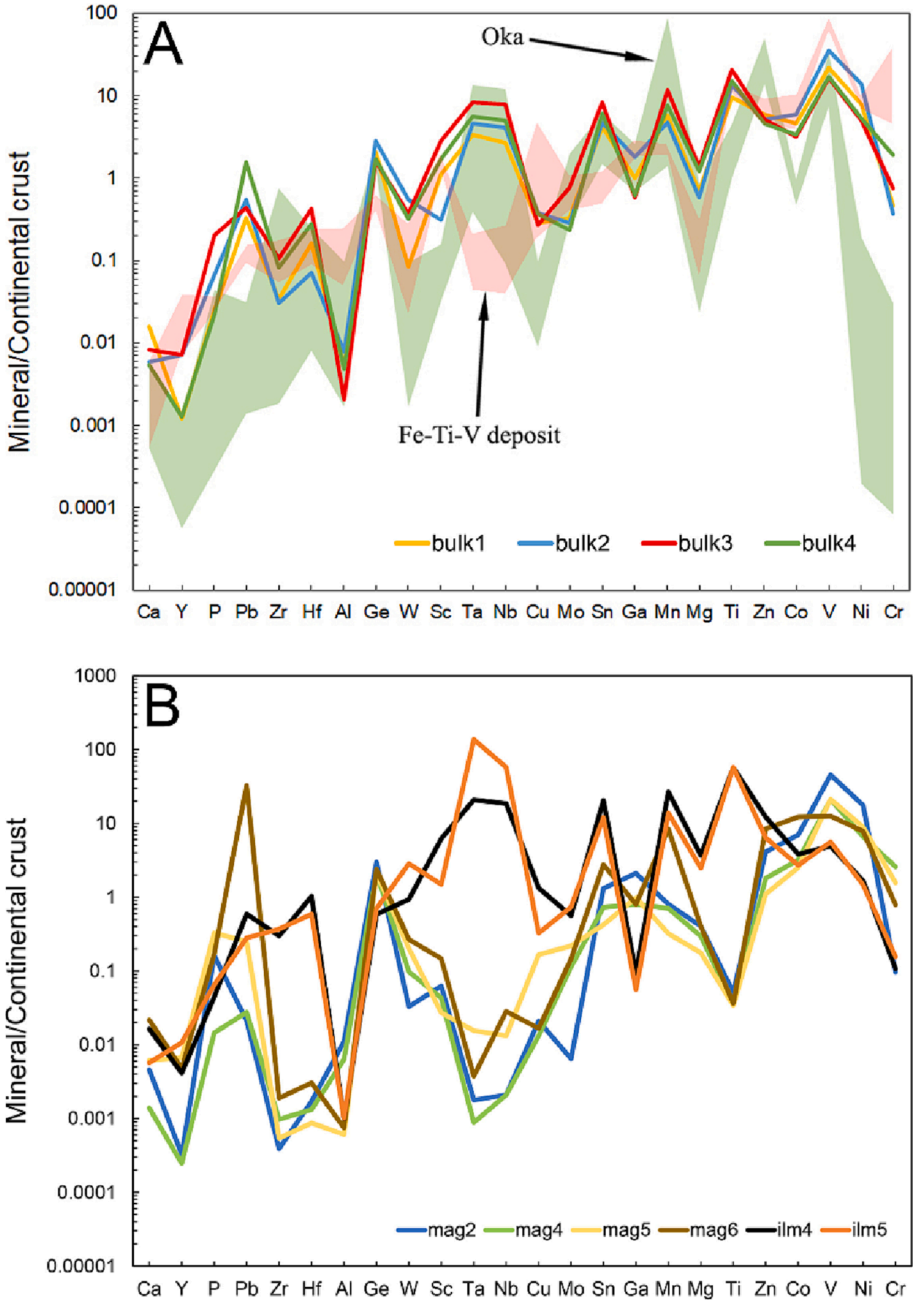

Fig. 6. Spider diagrams of the average concentrations of minor and trace element in each group of bulk Fe-Ti oxide (A) and magnetite and ilmenite (B) from the Tiechagou carbonatite. The normalization values are from Rudnick and Gao (2003). Data represented for Oka and Fe-Ti-V deposit refer to Chen et al. (2019) and Dare et al. (2014).

Table 2
Trace element compositions (ppm) of bulk Fe-Ti oxide, magnetite and ilmenite from the Tiechagou carbonatite-related iron deposit.

Sample	bulk Fe-Ti oxide						magnetite							
Type	bulk1 (n = 24)			bulk2 (n = 16)			bulk3 (n = 10)			buk4 (n = 10)			mag2 (n = 9)	
	Min	Max	Average	Min	Max	Average	Min	Max	Average	Min	Max	Average	Min	Max
Li	2.57	8.50	4.95	9.94	22.2	15.3	3.70	14.5	6.39	4.33	10.4	7.85	6.47	9.56
Na	b.d.	392	36.8	b.d.	364	106	5.98	87.8	32.8	b.d.	18.6	8.86	b.d.	41.2
Mg	9482	34,956	19,669	9024	25,897	16,330	24,840	68,921	38,393	36,091	64,731	52,634	10,818	11,886
Al	278	902	426	440	978	657	77.1	310	174	b.d.	1453	295	897	973
P	b.d.	52.5	10.8	b.d.	73.4	29.8	b.d.	376	88.6	b.d.	133	40.3	5.49	182
K	b.d.	b.d.	b.d.	b.d.	0.03	0.01	b.d.	b.d.	b.d.	b.d.	746	86.9	b.d.	215
Ca	b.d.	1983	166	b.d.	723	272	40.8	1499	381	b.d.	372	113	b.d.	875
Sc	7.09	49.9	24.3	2.89	12.3	6.88	34.4	145	62.5	63.4	112	88.5	0.77	2.16
Ti	11,368	113,931	52,010	27,588	130,284	73,347	58,333	230,824	111,877	115,094	208,569	166,709	238	335
V	2391	4499	3025	4142	5565	4884	1439	2740	2295	1656	2257	1937	5990	6468
Cr	24.7	372	62.7	5.54	270	50.0	59.0	200	102	35.2	102	57.3	7.77	18.8
Mn	1435	8407	4432	1658	6145	3674	5259	17,424	9090	9153	16,013	13,046	574	653
Co	76.4	193	124	122	182	158	69.0	103	85.6	75.5	98.4	89.8	182	192
Ni	349	767	464	554	967	823	168	387	295	190	301	247	1004	1088
Cu	0.34	95.0	7.84	1.85	44.5	10.3	2.18	12.9	7.39	b.d.	7.50	4.91	b.d.	2.16
Zn	217	842	434	194	970	366	248	653	373	243	473	347	225	332
Ga	12.2	27.5	15.9	22.1	33.8	29.2	4.89	11.6	9.40	b.d.	9.85	7.01	32.3	35.9
Ge	1.78	4.18	2.70	2.32	5.28	3.73	0.97	2.57	2.08	1.56	2.47	1.99	2.66	5.57
Rb	b.d.	1.07	0.10	0.00	1.46	0.43	b.d.	0.32	0.13	b.d.	1.32	0.14	b.d.	0.68
Sr	0.24	17.5	2.42	0.38	6.79	3.28	1.24	107	15.7	1.05	3.62	2.05	0.09	2.47
Y	b.d.	0.05	0.02	0.00	0.50	0.14	0.03	0.53	0.14	0.04	0.46	0.10	b.d.	0.03
Zr	1.14	14.2	4.49	1.37	8.32	4.05	5.09	51.7	13.9	0.0	25.2	16.0	b.d.	0.29
Nb	4.75	46.7	21.3	13.6	64.7	32.6	34.4	138	64.0	61.8	145	114	b.d.	0.12
Mo	0.09	0.59	0.27	0.06	0.45	0.23	0.32	1.48	0.62	0.28	0.58	0.43	b.d.	0.05
In	0.01	0.15	0.07	0.02	0.27	0.07	0.06	0.23	0.11	0.11	0.19	0.15	0.01	0.05
Sn	2.90	15.4	7.23	3.46	14.6	7.99	9.29	24.8	14.0	24.2	37.7	30.9	1.57	2.68
Cs	b.d.	0.07	0.01	b.d.	0.19	0.04	b.d.	0.02	0.01	b.d.	0.07	0.01	b.d.	0.05
Ba	0.18	8.64	1.43	1.64	21.5	6.68	0.80	104	13.8	0.67	4.10	1.73	0.23	9.84
La	b.d.	0.57	0.10	0.04	1.15	0.44	0.09	0.62	0.33	0.03	0.85	0.26	b.d.	0.12
Ce	0.04	0.79	0.26	0.09	2.21	0.72	0.10	0.73	0.46	0.08	1.00	0.34	b.d.	0.07
Hf	0.13	1.35	0.60	0.10	0.50	0.26	0.81	3.17	1.57	1.85	3.61	2.68	b.d.	0.02
Ta	0.55	5.08	2.36	0.95	6.69	3.20	3.01	11.5	5.78	2.67	10.2	7.05	b.d.	b.d.
W	b.d.	0.24	0.08	b.d.	2.93	0.56	b.d.	1.08	0.37	b.d.	b.d.	b.d.	b.d.	0.18
Pb	0.10	37.5	3.59	0.56	70.0	6.08	0.50	22.2	4.89	0.30	1.10	0.65	0.02	0.56

Note: b.d. represents analyses below detection limit, elements with compositions below detection limits are not shown.

The yielded temperature range of 999-1033 °C for the investigated Fe-Ti oxide (Type1 to Type4) is higher than the original titanomagnetite formation temperature (820 °C) obtained in the Damiao Fe-Ti-(P) ore deposit located within the North China Craton (Wei et al., 2020a, Wei et al., 2020b).

The ilmenite and magnetite evolution history in the Tiechagou carbonatite is developed based on the following evidences, including (1) the micro-texture showing that thin lamellae ilmenite oxy-exsolutions (Type1) occur together with thick ilmenite lamellae (Type2), and also demonstrating the similar occurrences for fine- and coarse-grained granular ilmenite oxy-exsolutions (Type3 and Type4; Fig. 3); (2) the geochemical data showing similar elemental concentrations and trends for bulk Fe-Ti oxides (Fig. 5A, 6A), which indicates origin from the same parental titanomagnetite; (3) the calculated physicochemical parameters of the Fe-Ti oxide pairs showing a correlated decrease in temperature and oxygen fugacity from magnetite hosting thin lamellae ilmenite oxy-exsolutions (Type1) to magnetite hosting thick lamellae ilmenite oxy-exsolutions (Type2), whereas an increase in oxygen fugacity from magnetite hosting fine-grained granular ilmenite oxy-exsolutions (Type3) to magnetite hosting coarse-grained granular ilmenite oxy-exsolutions (Type4) at a relatively constant temperature (Figs. 9 and 10). The above-outlined evidences help to formulate our ilmenite-magnetite evolution in two almost simultaneous oxy-exsolution processes. The first model starts by the oxidation of titanomagnetite above the solvus temperature that results in the formation of Type1 Fe-Ti oxide intergrowth. As temperature and oxygen fugacity drop, the thin ilmenite lamellae in magnetite (Type1) evolves to form thick lamellae generations (Type2; Figs. 9 and 10). The remarkable drop in oxygen fugacity from Type1 to Type2 is consistent with the depletion of MnO in Fe-Ti oxides (Reguir et al., 2008). The correlated decrease of temperature and oxygen fugacity is commonly observed for the petrogenesis of magnetite and ilmenite assemblages in magmatic Fe-Ti-V deposits, including Emeishan and Damiao (Liu et al., 2015; Wei et al., 2020a, Wei et al., 2020b). The second model is driven by the oxidation of titanomagnetite below the solvus temperature, fine-grained ilmenite oxy-exsolution in magnetite forms involving the slight drop in temperature in the range of approximately 500–400 °C, and coarse-grained ilmenite oxy-exsolution generates as the oxygen fugacity ($logfO_2$) increases from −28.38 to −26.93 (on average; Figs. 9 and 10). The increasing oxygen fugacity at a subsolvus temperature results in extensive oxidation and favours the formation of granular ilmenite oxy-exsolutions. Of note, it is worthy to highlight the importance of cooling rate in the formation of lamellae and granular ilmenite oxy-exsolutions from the original titanomagnetite (Price, 1979). In this respect, we used the isopleths of Fe-Ti oxides solid solution established by Frost (1991) and modified after Tan et al. (2022). Our modelling data indicate that Usp0.05Mag0.95 and Ilm0.79Hem0.21 can crystallize simultaneously at 683 °C and FMQ + 2.74 (point “a” in Fig. 11) resulting in the oxy-exsolutions of lamellae ilmenite hosted by magnetite (type1) in the model A, whereas co-crystallization of Usp0.05Mag0.95 and Ilm0.97Hem0.03 occurs at 514 °C and FMQ-1.98 (point “b” in Fig. 11) following the oxidation of titanomagnetite and give rise to the magnetite hosting fine granular

										ilmenite					
	mag4 (n = 9)			mag5 (n = 11)			mag6 (n = 41)			ilm4 (n = 21)			ilm5 (n = 14)		
Average	Min	Max	Average	Min	Max	Average	Min	Max	Average	Min	Max	Average	Min	Max	Average
7.68	1.69	4.58	2.65	2.48	4.47	3.62	0.21	3.27	1.51	3.22	13.5	7.73	23.2	66.8	55.1
12.2	b.d.	87.3	14.9	b.d.	88.4	17.7	b.d.	11,198	621	b.d.	119	46.9	1.67	166	44.8
11,449	7602	9073	8401	3914	6267	5001	2837	45,022	11,378	49,655	126,258	104,271	62,746	84,701	70,146
931	164	891	533	8.17	140	51.1	b.d.	586	62.9	12.4	382	83.8	0.50	1030	85.0
70.7	b.d.	27.7	6.33	b.d.	612	144	b.d.	1404	74.4	b.d.	75.0	19.5	b.d.	171	28.2
51.4	15.2	518	122	b.d.	70.5	17.7	b.d.	b.d.	b.d.	b.d.	b.d.	b.d.	b.d.	b.d.	b.d.
208	b.d.	236	63.3	b.d.	2676	280	b.d.	6414	990	b.d.	8205	748	b.d.	2528	261
1.37	0.80	1.22	0.94	0.13	0.95	0.59	0.35	8.63	3.22	44.8	192	136	28.6	36.6	32.7
277	144	239	192	110	272	185	1.64	743	197	118,963	343,372	308,271	262,819	343,596	312,786
6269	2844	2969	2916	2399	3556	2931	547	3634	1735	418	1684	677	550	1390	777
13.1	191	455	348	28.9	458	212	3.79	780	106	0.71	83.4	14.4	5.09	43.7	21.0
622	501	617	547	168	359	250	2800	10,165	6532	7925	28,417	20,712	9206	15,614	10,728
185	76.7	92.7	84.9	32.1	97.0	66.9	179	472	325	56.7	115	102	45.8	93.6	72.0
1038	354	414	390	324	965	526	243	1237	461	44.4	320	98.1	46.9	171	86.8
0.56	0.03	0.89	0.36	b.d.	17.3	4.50	b.d.	8.03	0.45	3.04	472	35.8	4.29	32.2	8.79
296	73.5	166	130	41.3	127	79.5	67.1	1955	609	429	1561	882	256	657	460
33.8	12.2	13.9	12.8	12.8	17.2	15.7	1.49	63.8	12.8	0.27	9.13	1.49	0.25	4.25	0.89
3.88	2.02	3.61	2.73	1.86	4.25	2.77	0.82	6.19	3.10	b.d.	2.33	0.76	0.45	1.67	0.91
0.16	b.d.	1.17	0.26	b.d.	1.01	0.19	b.d.	5.38	0.28	b.d.	0.36	0.13	b.d.	3.38	0.36
0.66	0.08	6.37	1.06	0.01	19.5	2.50	b.d.	44.8	4.81	0.50	217	18.0	0.37	12.0	2.68
0.01	b.d.	0.01	b.d.	b.d.	1.23	0.13	b.d.	0.74	0.09	0.01	0.31	0.08	0.01	1.70	0.20
0.05	0.01	0.31	0.13	b.d.	0.21	0.07	b.d.	3.7	0.25	17.0	70.2	39.5	14.1	129	48.8
0.02	b.d.	0.05	0.02	b.d.	0.41	0.11	b.d.	6.01	0.23	46.2	249	149	178	612	461
0.01	b.d.	0.23	0.09	0.01	0.61	0.17	b.d.	0.44	0.12	0.04	1.61	0.45	0.28	1.21	0.59
0.03	b.d.	0.02	0.01	b.d.	0.02	b.d.	b.d.	0.20	0.04	0.15	0.47	0.32	0.14	0.31	0.22
2.23	0.94	1.43	1.24	0.27	1.05	0.72	0.21	19.6	4.71	16.0	41.6	34.8	15.0	30.1	20.4
0.01	b.d.	0.01	b.d.	b.d.	0.05	0.02	b.d.	1.00	0.05	b.d.	0.13	0.02	b.d.	0.15	0.03
2.78	0.44	15.7	2.80	b.d.	3.90	0.83	b.d.	16.6	1.72	0.04	3.26	0.97	b.d.	3.90	1.14
0.04	b.d.	0.02	0.01	b.d.	1.64	0.24	b.d.	0.87	0.14	0.03	1.37	0.51	0.01	1.02	0.48
0.02	b.d.	0.03	0.01	0.01	3.14	0.43	b.d.	1.91	0.27	0.03	2.17	0.71	0.17	1.52	0.80
0.01	b.d.	0.01	b.d.	b.d.	0.01	0.00	b.d.	0.08	0.01	1.33	5.97	3.81	1.47	3.02	2.18
b.d.	b.d.	b.d.	b.d.	b.d.	0.04	0.01	b.d.	b.d.	b.d.	3.89	23.4	14.6	21.5	205	96.4
0.03	b.d.	0.38	0.10	b.d.	1.34	0.20	b.d.	2.93	0.27	0.01	1.89	0.93	1.36	4.49	2.85
0.23	0.05	0.90	0.30	0.02	17.1	2.75	0.11	3519	358	0.04	51.9	6.51	0.11	15.7	3.09

ilmenite (type2) in the model B.

Lamellae and granular ilmenite hosted by magnetite is formed via oxidation of magnetite- ulvöspinel assemblages through the classic reaction with oxygen as the oxidizing agent (Buddington and Lindsley, 1964):

$$3Fe_2^{2+}TiO_4 + \frac{1}{2}O_2 \leftrightarrow 3Fe^{2+}TiO_3 + Fe_2^{3+}Fe^{2+}O_4 \quad (1)$$

This reaction is very common in magnetite from igneous and metamorphic rocks and magmatic Fe-Ti oxide and iron skarn deposits (Hu et al., 2015; Tan et al., 2016; Huang et al., 2019). Recently, Brzozowski et al. (2020) proposed that CO_2 can also serve as an important oxidizing agent for the oxidation of magnetite-ulvöspinel assemblages:

$$9Fe_2^{2+}TiO_4 + 0.75CO_2 + 1.5H_2O \leftrightarrow 9Fe^{2+}TiO_3 + 3Fe_2^{3+}Fe^{2+}O_4 + 0.75CH_4 \quad (2)$$

Carbon in the oxidized form (e.g., CO_2 or CO_3^{2-}) within carbonatite systems probably also plays a significant role as the oxidizing agent especially when the oxygen fugacity is decreasing and low, i.e., in the first model that forms the thick lamellae ilmenite exsolutions. This might be a common scenario in C-bearing systems especially carbonatite associated alkaline complexes as identified here and others (e.g., Phalaborwa and Kovdor; Ivanyuk et al., 2016; Milani et al., 2017).

Here we consider that complete oxidation of ulvöspinel took place in the Tiechagou carbonatite, which leads to the formation of thin trellis ilmenite (model1; Type1 and Type2). This is evidenced by the onset temperature of 683 °C in Type1. Duchesne (1970) has also claimed the formation of trellis lamellae at the supersolvus temperature due to the complete oxidation of ulvöspinel. Another evidence showing the complete oxidation is the absence of cloth intergrowth of ulvöspinel-magnetite in all investigated samples (Duchesne, 1970). On the other hand, we think that the granular ilmenite oxy-exsolutions (model2; Type3 and Type4) form through subsolvus oxidation demonstrated by their onset temperature of 514 °C in Type3. In both models, the increasing degree of diffusion also influences the change of the ilmenite texture from thin to thick (model1) and fine-grained to coarse-grained (model2).

6. Conclusions

Micro-texture, geochemistry and thermo-oxybarometry of various ilmenite-magnetite intergrowths from the Tiechagou carbonatite have been investigated in this study. Geochemical compositions generally record higher contents of Mg, Ti and Mn in the earlier generations (Type1 and Type3) and lower contents of these elements in the more evolved generations (Type2 and Type4), whereas minor and trace elements show similar concentrations and trends for the bulk Fe-Ti oxides confirming crystallization from a common parental ulvöspinel-magnetite assemblage. PCA was performed on both magnetite and ilmenite elemental compositions and successfully discriminated different magnetite (mag2, mag4, mag5 and mag6) and ilmenite groups (ilm4 and ilm5). Furthermore, thermo-oxybarometric data show that the earliest generation (Type1) is characterized by the highest temperature and oxygen fugacity. Based on the combined geochemical, statistical and thermo-oxybarometric features, the Fe-Ti oxides within Tiechagou carbonatites are evolved from the original titanomagnetite (999-1033 °C)

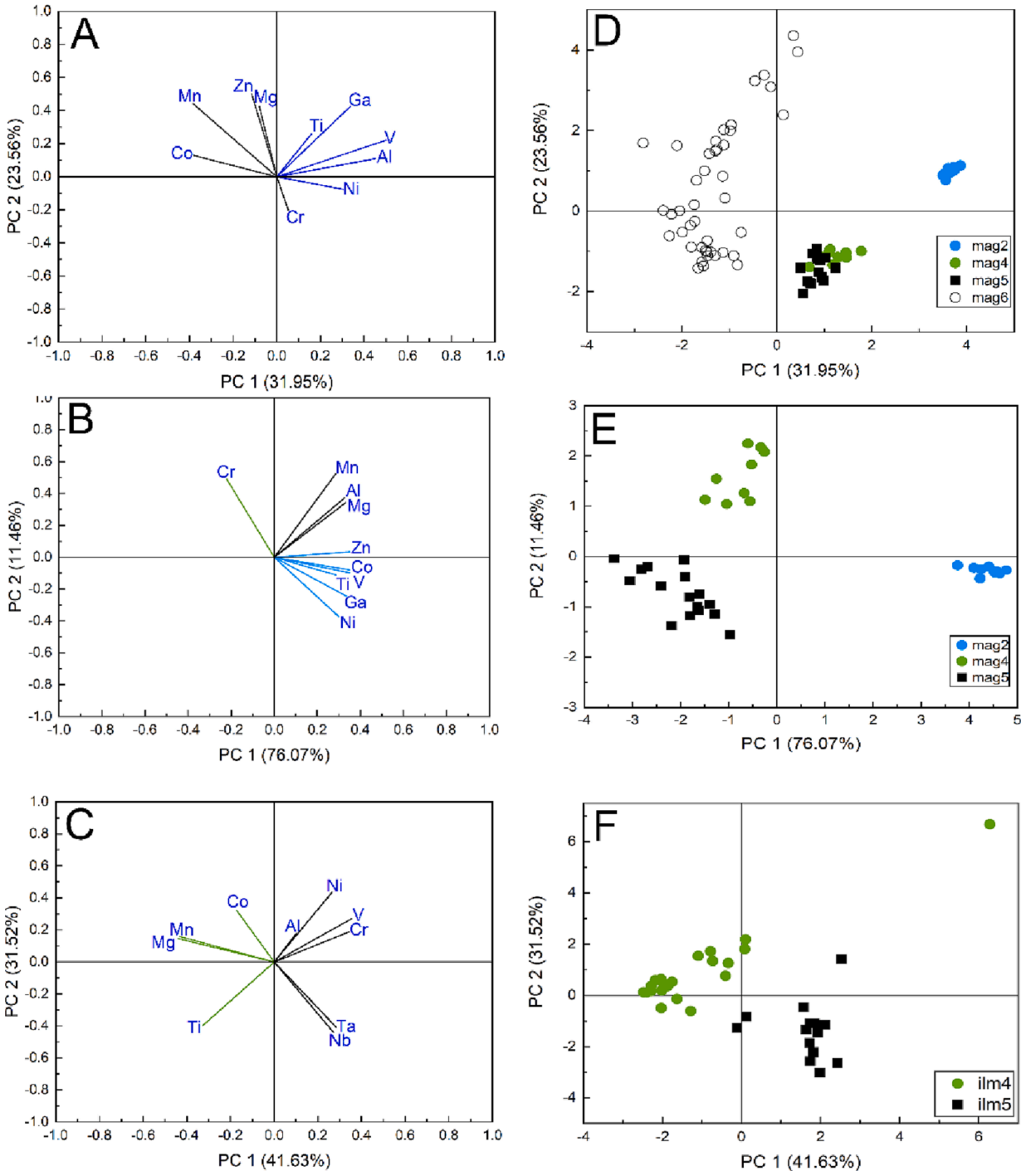

Fig. 7. Principal component analysis (PCA) of geochemical data of magnetite and ilmenite from the Tiechagou carbonatite. Loadings (A-C) and scores (D-F) of the first and second principal components are shown.

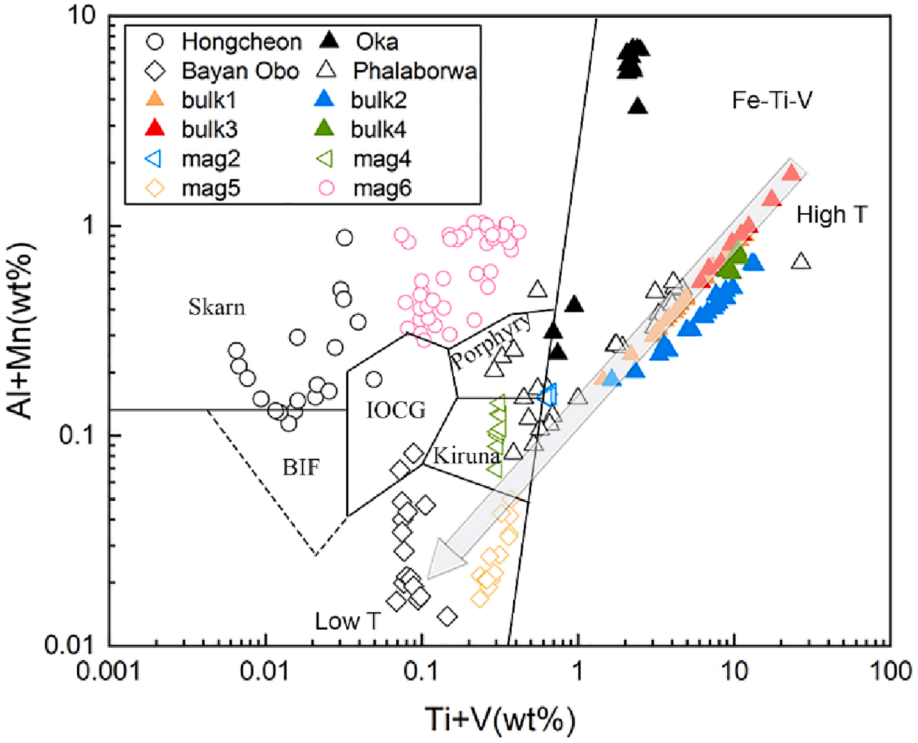

Fig. 8. Binary diagram of Al + Mn versus Ti + V in magnetite. Data represented for Hongcheon, Bayan Obo and Oka deposit refer to Chen et al. (2019). Phalaborwa data are adopted from Milani et al. (2017).

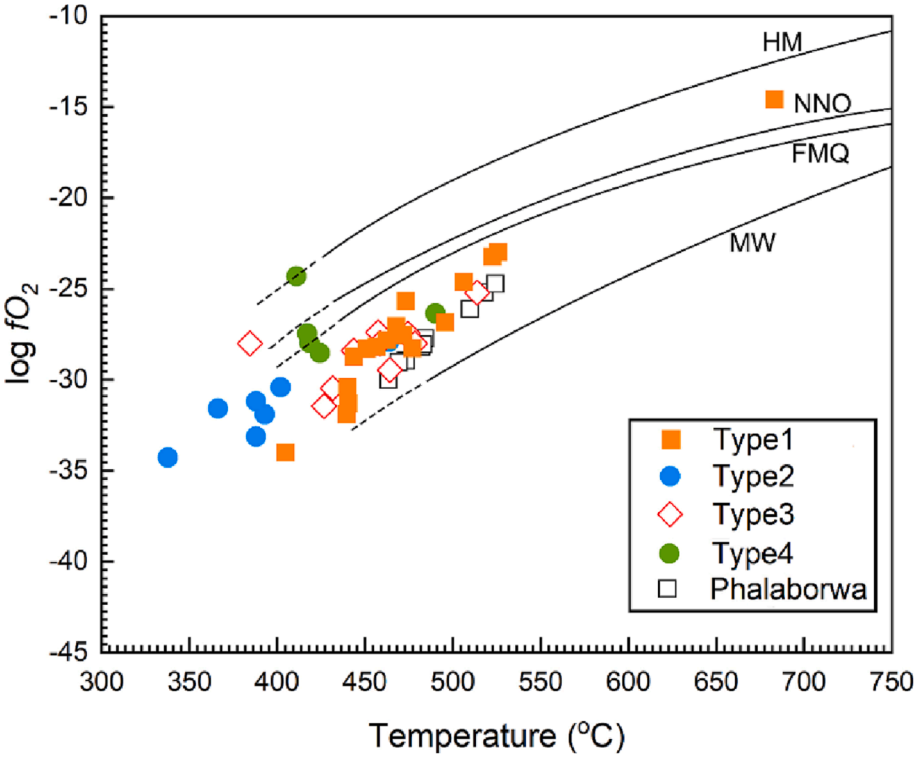

Fig. 9. Temperature and oxygen fugacity re-equilibration diagram of different magnetite and ilmenite pairs. Phalaborwa data are taken from Milani et al. (2017). Abbreviations are the fugacity buffers: FMQ, fayalite-magnetite-quartz; HM, hematite-magnetite; MW, magnetite-wustite; NNO, nickel-nickel oxide.

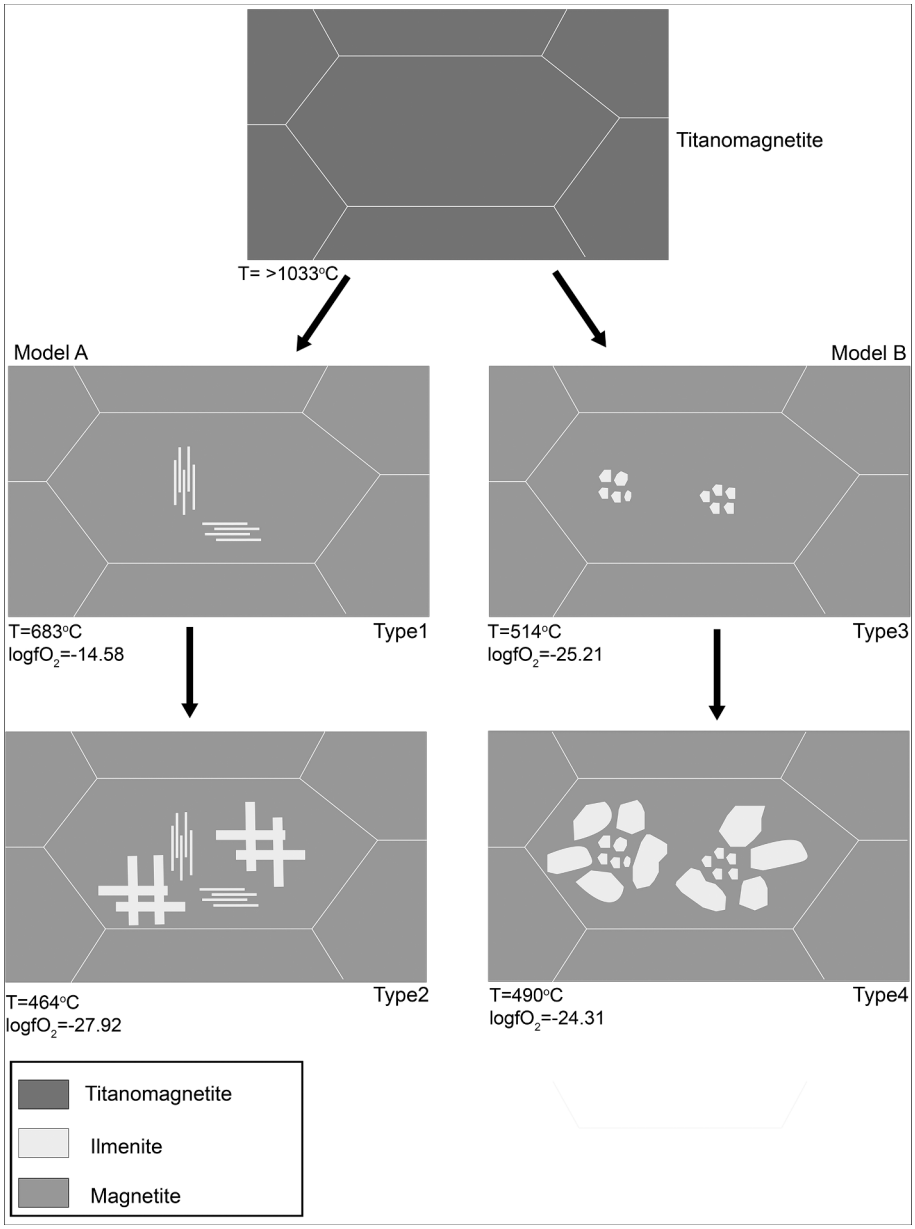

Fig. 10. The genetic model of associated ilmenite and magnetite evolution history in the Tiechagou carbonatite. The titanomagnetite formation temperature is estimated adopting the $T_{Mg\text{-}Mag}$ geothermometer established by Canil and Lacourse (2020). Temperature shown in the model descriptions represent the starting value identified in each type together with the highest oxygen fugacity listed.

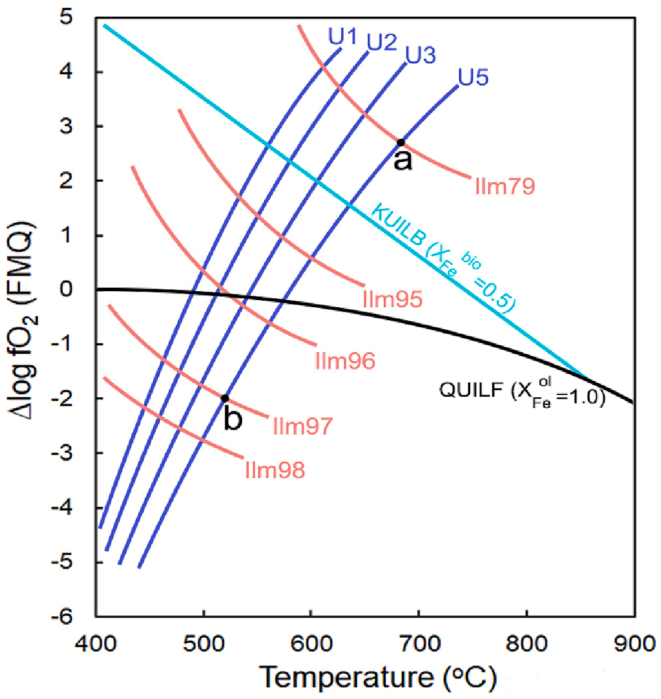

Fig. 11. The diagram of Δlog fO_2 (FMQ) vs. T showing the isopleths of Fe-Ti oxide solid solution (modified after Frost (1991) and Tan et al. (2022)). Oxygen fugacity and temperature determined by QUILF-95 at P = 5 kbar; U5 refers to solid solution of ulvöspinel5 – magnetite95 (in molar fraction) and Ilm80 refers to ilmenite80 – hematite20; Δlog fO_2 refers to the FMQ buffer; "a" refers to the co-crystallization T-fO_2 condition for U0.05Mag95 and Ilm0.79Hem0.21, "b" refers to the T-fO_2 condition for co-crystallization of U0.05Mag0.95 and Ilm0.97Hem0.03.

in the following two models. In the first model, titanomagnetite, starting at a supersolvus temperature, evolves to magnetite hosting thin and thick lamellae ilmenite due to a progressive decrease of both temperature and oxygen fugacity. In the second model, titanomagnetite evolves to magnetite hosting fine- and coarse-grained granular ilmenite oxy-exsolutions through subsolvus oxidation caused by increasing oxygen fugacity with slightly decreasing temperature. Carbon in the oxidized form serves as the oxidizing agent when the oxygen fugacity is low and/or decreasing within carbonatite systems.

Declaration of Competing Interest

The authors declare that they have no known competing financial interests or personal relationships that could have appeared to influence the work reported in this paper.

Data availability

The data that has been used is confidential.

Acknowledgements

This study was supported financially by the National Key R&D Program of China (No. 2019YFA0708400), the National Natural Science Foundation of China (No. 41973016), and the special fund from the State Key Laboratory of Geological Processes and Mineral Resources (No. MSFGPMR03-2).

Appendix A. Supplementary data

Supplementary data to this article can be found online at https://doi.org/10.1016/j.oregeorev.2023.105439.

References

Arguin, J.P., Pagé, P., Barnes, S.J., Girard, R., Duran, C., 2018. An integrated model for ilmenite, Al-spinel, and corundum exsolutions in titanomagnetite from oxide-rich layers of the Lac Doré complex (Québec, Canada). Minerals 8, 476. https://doi.org/10.3390/min8110476.

Bai, T., Chen, W., Jiang, S.Y., 2019. Evolution of the carbonatite Mo-HREE deposits in the Lesser Qinling Orogen: Insights from in situ geochemical investigation of calcite and sulfate. Ore Geol. Rev. 113, 103069 https://doi.org/10.1016/j.oregeorev.2019.103069.

Bailey, D.K., Kearns, S., 2002. High-Ti magnetite in some fine-grained carbonatites and the magmatic implications. Mineral. Mag. 66, 379–384. https://doi.org/10.1180/0026461026630035.

Brzozowski, M.J., Samson, I.M., Gagnon, J.E., Linnen, R.L., Good, D.J., 2020. Effects of fluid-induced oxidation on the composition of Fe–Ti oxides in the Eastern Gabbro, Coldwell Complex, Canada: implications for the application of Fe–Ti oxides to petrogenesis and mineral exploration. Miner. Deposita 56, 601–618. https://doi.org/10.1007/s00126-020-00988-4.

Buddington, A.F., Lindsley, D.H., 1964. Iron-titanium oxide minerals and synthetic equivalents. J. Petrol. 5, 310–357. https://doi.org/10.1093/petrology/5.2.310.

Canil, D., Grondahl, C., Lacourse, T., Pisiak, L.K., 2016. Trace elements in magnetite from porphyry Cu-Mo-Au deposits in British Columbia. Canada. Ore Geol. Rev. 72, 1116–1128. https://doi.org/10.1016/j.oregeorev.2015.10.007.

Canil, D., Lacourse, T., 2020. Geothermometry using minor and trace elements in igneous and hydrothermal magnetite. Chem. Geol. 541, 119576 https://doi.org/10.1016/j.chemgeo.2020.119576.

Charlier, B., Skår, Ø., Korneliussen, A., Duchesne, J.C., Vander Auwera, J., 2007. Ilmenite composition in the Tellnes Fe-Ti deposit, SW Norway: Fractional crystallization, postcumulus evolution and ilmenite-zircon relation. Contrib. Mineral. Petrol. 154, 119–134. https://doi.org/10.1007/s00410-007-0186-8.

Chen, W., Ying, Y.C., Bai, T., Zhang, J.J., Jiang, S.Y., Zhao, K.D., Shin, D., Kynicky, J., 2019. In situ major and trace element analysis of magnetite from carbonatite-related complexes: Implications for petrogenesis and ore genesis. Ore Geol. Rev. 107, 30–40. https://doi.org/10.1016/j.oregeorev.2019.01.029.

Dare, S.A.S., Barnes, S.J., Beaudoin, G., 2012. Variation in trace element content of magnetite crystallized from a fractionating sulfide liquid, Sudbury, Canada: Implications for provenance discrimination. Geochim. Cosmochim. Acta 88, 27–50. https://doi.org/10.1016/j.gca.2012.04.032.

Dare, S.A.S., Barnes, S.J., Beaudoin, G., Méric, J., Boutroy, E., Potvin-Doucet, C., 2014. Trace elements in magnetite as petrogenetic indicators. Miner. Deposita 49, 785–796. https://doi.org/10.1007/s00126-014-0529-0.

Dare, S.A.S., Barnes, S.J., Beaudoin, G., 2015. Did the massive magnetite "lava flows" of El Laco (Chile) form by magmatic or hydrothermal processes? New constraints from magnetite composition by LA-ICP-MS. Miner. Deposita 50, 607–617. https://doi.org/10.1007/s00126-014-0560-1.

Dong, Y., Santosh, M., 2016. Tectonic architecture and multiple orogeny of the Qinling Orogenic Belt, Central China. Gondwana Res. 29, 1–40. https://doi.org/10.1016/j.gr.2015.06.009.

Duchesne, J., 1970. Microtextures of Fe-Ti oxide minerals in the South-Rogaland Anorthositic Complex (Norway). Ann. Soc. Géol. Belg. 93, 527–544.

Dupuis, C., Beaudoin, G., 2011. Discriminant diagrams for iron oxide trace element fingerprinting of mineral deposit types. Miner. Deposita 46, 319–335. https://doi.org/10.1007/s00126-011-0334-y.

Duran, C.J., Barnes, S.J., Mansur, E.T., Dare, S.A.S., Bédard, L.P., Sluzhenikin, S.F., 2020. Magnetite chemistry by LA-ICP-MS records sulfide fractional crystallization in massive nickel-copper-platinum group element ores from the Norilsk-Talnakh Mining District (Siberia, Russia): implications for trace element partitioning into magnetite. Econ. Geol. 115, 1245–1266. https://doi.org/10.5382/econgeo.4742.

Frost, B.R., 1991. Magnetic petrology: factors that control the occurrence of magnetite in crustal rocks. Rev. Mineral. Geochem. 25, 489–509.

Gaspar, J.C., Wyllie, P.J., 1983a. Ilmenite (high Mg, Mn, Nb) in the carbonatites from the Jacupiranga complex. Brazil. Am. Mineral. 68, 960–971.

Gaspar, J.C., Wyllie, P.J., 1983b. Magnetite in the carbonatites from the Jacupiranga complex. Brazil. Am. Mineral. 68, 960–971.

Ghiorso, M.S., Sack, R.O., 1991. Thermochemistry of the oxide minerals. Rev. Mineral. 25, 221–264.

Guzmics, T., Mitchell, R.H., Szabó, C., Berkesi, M., Milke, R., Abart, R., 2011. Carbonatite melt inclusions in coexisting magnetite, apatite and monticellite in Kerimasi calciocarbonatite, Tanzania: Melt evolution and petrogenesis. Contrib. Mineral. Petrol. 161, 177–196. https://doi.org/10.1007/s00410-010-0525-z.

Haggerty, S.E., 1995. Upper mantle mineralogy. J. Geodyn. 20, 331–364. https://doi.org/10.1016/0264-3707(95)00016-3.

Hu, Z.C., Gao, S., Liu, Y.S., Hu, S.H., Chen, H.H., Yuan, H.L., 2008. Signal enhancement in laser ablation ICP-MS by addition of nitrogen in the central channel gas. J. Anal. At. Spectrom. 23, 1093–1101. https://doi.org/10.1039/b804760j.

Hu, H., Lentz, D., Li, J.W., McCarron, T., Zhao, X.F., Hall, D., 2015. Reequilibration processes in Magnetite from Iron Skarn Deposits. Econ. Geol. 110, 1–8. https://doi.org/10.2113/econgeo.110.1.1.

Hu, H., Li, J.W., Harlov, D.E., Lentz, D.R., McFarlane, C.R.M., Yang, Y.H., 2020. A Genetic Link between Iron Oxide-Apatite and Iron Skarn Mineralization in the Jinniu Volcanic Basin, Daye District, Eastern China: Evidence from Magnetite Geochemistry and Multi-Mineral U-Pb Geochronology. GSA Bull. 132, 899–917. https://doi.org/10.1130/B35180.1.

Huang, X.W., Zhou, M.F., Qiu, Y.Z., Qi, L., 2015. In-situ LA-ICP-MS trace elemental analyses of magnetite: The Bayan Obo Fe-REE-Nb deposit, North China. Ore Geol. Rev. 65, 884–899. https://doi.org/10.1016/j.oregeorev.2014.09.010.

Huang, X.W., Sappin, A.A., Boutroy, E., Beaudoin, G., Makvandi, S., 2019. Trace element composition of igneous and hydrothermal magnetite from porphyry deposits: Relationship to deposit subtypes and magmatic affinity. Econ. Geol. 114, 917–952. https://doi.org/10.5382/econgeo.4648.

Ivanyuk, G.Y., Kalashnikov, A.O., Pakhomovsky, Y.A., Mikhailova, J.A., Yakovenchuk, V. N., Konopleva, N.G., Sokharev, V.A., Bazai, A.V., Goryainov, P.M., 2016. Economic minerals of the Kovdor baddeleyite-apatite-magnetite deposit, Russia: Mineralogy, spatial distribution and ore processing optimization. Ore Geol. Rev. 77, 279–311. https://doi.org/10.1016/j.oregeorev.2016.02.008.

Jang, Y.D., Naslund, H.R., 2003. Major and trace element variation in ilmenite in the Skaergaard Intrusion: Petrologic implications. Chem. Geol. 193, 109–125. https://doi.org/10.1016/S0009-2541(02)00224-3.

Jian, W., Lehmann, B., Mao, J., Ye, H., Li, Z., He, H., Zhang, J., Zhang, H., Feng, J., 2015. Mineralogy, fluid characteristics, and Re-Os age of the late triassic Dahu Au-Mo deposit, Xiaoqinling Region, Central China: Evidence for a magmatic-hydrothermal origin. Econ. Geol. 110, 119–145. https://doi.org/10.2113/econgeo.110.1.119.

Kroner, A., Compston, W., Zhang, G.W., Guo, A.L., Todt, W., 1988. Age and tectonic setting of Late Archean greenstone-gneiss terrain in Henan Province, China, as revealed by single-grain zircon dating. Geology 16, 211–215.

Lee, M.J., Lee, J.I., Moutte, J., 2005. Compositional variation of Fe-Ti oxides from the Sokli complex, northeastern Finland. Geosci. J. 9, 1–13. https://doi.org/10.1007/BF02910549.

Lepage, L.D., 2003. ILMAT: An Excel worksheet for ilmenite-magnetite geothermometry and geobarometry. Comput. Geosci. 29, 673–678. https://doi.org/10.1016/S0098-3004(03)00042-6.

Lilova, K.I., Pearce, C.I., Gorski, C., Rosso, K.M., Navrotsky, A., 2012. Thermodynamics of the magnetite-ulvöspinel (Fe3O4-Fe2TiO4) solid solution. Am. Mineral. 97, 1330–1338. https://doi.org/10.2138/am.2012.4076.

Lindsley, D.H., Epler, N., 2017. Do Fe-Ti-oxide magmas exist? Probably not! Am. Mineral. 102, 2157–2169. https://doi.org/10.2138/am-2017-6091.

Liu, Y.S., Hu, Z.C., Gao, S., Günther, D., Xu, J., Gao, C.G., Chen, H.H., 2008. In situ analysis of major and trace elements of anhydrous minerals by LA-ICP-MS without applying an internal standard. Chem. Geol. 257, 34–43. https://doi.org/10.1016/j.chemgeo.2008.08.004.

Liu, P.P., Zhou, M.F., Chen, W.T., Gao, J.F., Huang, X.W., 2015. In-situ LA-ICP-MS trace elemental analyses of magnetite: Fe-Ti-(V) oxide-bearing mafic-ultramafic layered intrusions of the Emeishan Large Igneous Province, SW China. Ore Geology Reviews 65, 853–871.

Makvandi, S., Ghasemzadeh-Barvarz, M., Beaudoin, G., Grunsky, E.C., McClenaghan, M. B., Duchesne, C., 2016. Principal component analysis of magnetite composition from volcanogenic massive sulfide deposits: Case studies from the Izok Lake (Nunavut, Canada) and Halfmile Lake (New Brunswick, Canada) deposits. Ore Geol. Rev. 72, 60–85. https://doi.org/10.1016/j.oregeorev.2015.06.023.

Milani, L., Bolhar, R., Cawthorn, R.G., Frei, D., 2017. In situ LA–ICP-MS and EPMA trace element characterization of Fe–Ti oxides from the phoscorite–carbonatite association at Phalaborwa, South Africa. Miner. Deposita 52, 747–768. https://doi.org/10.1007/s00126-016-0696-2.

Mollo, S., Putirka, K., Iezzi, G., Scarlato, P., 2013. The control of cooling rate on titanomagnetite composition: Implications for a geospeedometry model applicable to alkaline rocks from Mt. Etna volcano. Contrib. Mineral. Petrol. 165, 457–475. https://doi.org/10.1007/s00410-012-0817-6.

Nadoll, P., Angerer, T., Mauk, J.L., French, D., Walshe, J., 2014. The chemistry of hydrothermal magnetite: A review. Ore Geol. Rev. 61, 1–32. https://doi.org/10.1016/j.oregeorev.2013.12.013.

Price, G.D., 1979. Microstructures in titanomagnetites as guides to cooling rates of a Swedish intrusion. Geol. Mag. 116, 313–318.

Ray, G.E., Webster, I.C.L., 2007. Geology and chemistry of the low Ti magnetite-bearing Heff Cu-Au skarn and its associated plutonic rocks, Heffley Lake, South-central British Columbia. Explor. Min. Geol. 16, 159–186. https://doi.org/10.2113/gsemg.16.3-4.159.

Reguir, E.P., Chakhmouradian, A.R., Halden, N.M., Yang, P., Zaitsev, A.N., 2008. Early magmatic and reaction-induced trends in magnetite from the carbonatites of Kerimasi, Tanzania. Can. Mineral. 46, 879–900. https://doi.org/10.3749/canmin.46.4.879.

Ripp, G.S., Karmanov, N.S., Doroshkevich, A.G., Badmatsyrenov, M.V., Izbrodin, I.A., 2006. Chrome-bearing mineral phases in the carbonatites of northern Transbaikalia. Geochem. Int. 44, 395–402. https://doi.org/10.1134/S0016702906040069.

Rudnick, R.L., Gao, S., 2003. Composition of the continental crust. In: Holland, H.D., Turekian, K.K. (Eds.), Treatise on Geochemistry, v. 3. Elsevier Ltd., pp. 1–64

Sack, R.O., 1982. Spinels as petrogenetic indicators: Activity-composition relations at low pressures. Contrib. Mineral. Petrol. 79, 169–186. https://doi.org/10.1007/BF01132886.

Sauerzapf, U., Lattard, D., Burchard, M., Engelmann, R., 2008. The titanomagnetite-ilmenite equilibrium: New experimental data and thermo-oxybarometric application to the crystallization of basic to intermediate rocks. J. Petrol. 49, 1161–1185. https://doi.org/10.1093/petrology/egn021.

Song, W.L., Xu, C., Smith, M., Kynicky, J., Huang, K.J., Wei, C.W., Zhou, L., Shu, Q.H., 2016. Origin of unusual HREE-Mo-rich carbonatites in the Qinling orogeny, China. Sci. Rep. 6, 37377. https://doi.org/10.1038/srep37377.

Spencer, K.J., Lindsley, D.H., 1981. A solution model for coexisting iron–titanium oxides. Am. Mineral. 66, 1189–1201.

Stein, H.J., Markey, R.J., Morgan, J.W., 1997. Highly precise and accurate Re-Os ages for molybdenite from the East Qinling molybdenum belt, Shaanxi Province. China. Econ. Geol. 92, 827–835.

Tan, W., Liu, P., He, H.P., Wang, C.Y., Liang, X.L., 2016. Mineralogy and origin of exsolution in Ti-rich magnetite from different magmatic Fe-Ti oxide-bearing intrusions. Can. Mineral. 54, 539–553. https://doi.org/10.3749/canmin.1400069.

Tan, W., Wang, C.Y., Reddy, S.M., He, H.P., Xian, H.Y., Xing, C.M., 2022. Magnetite-rutile symplectite in ilmenite records magma hydration in layered intrusions. Am. Mineral. 107, 395–404. https://doi.org/10.2138/am-2021-7777.

Taylor, R.W., 1964. Phase equilibria in the system FeO-Fe_2O_3-TiO_2 at 1300 °C. Am. Mineral. 49, 1016–1030.

Verdugo-Ihl, M.R., Ciobanu, C.L., Cook, N.J., Ehrig, K., Slattery, A., Courtney-Davies, L., Dmitrijeva, M., 2021. Nanomineralogy of hydrothermal magnetite from Acropolis, South Australia: Genetic implications for iron-oxide copper gold mineralization. Am. Mineral. 106, 1273–1293. https://doi.org/10.2138/am-2021-7557.

Von Gruenewaldt, G., Klemm, D.D., Henckel, J., Dehm, R.M., 1985. Exsolution features in titanomagnetites from massive magnetite layers and their host rocks of the upper zone, eastern Bushveld Complex. Econ. Geol. 80, 1049–1061. https://doi.org/10.2113/gsecongeo.80.4.1049.

Wang, C.M., He, X., Carranza, E.J.M., Cui, C., 2019. Paleoproterozoic volcanic rocks in the southern margin of the North China Craton, central China: Implications for the Columbia supercontinent. Geosci. Front. 10, 1543–1560. https://doi.org/10.1016/j.gsf.2018.10.007.

Wei, Y.Q., Niu, Y.L., Gong, H.M., Duan, M., Chen, S., Guo, P.Y., Sun, P., 2020b. Geochemistry and iron isotope systematics of coexisting Fe-bearing minerals in magmatic Fe Ti deposits: A case study of the Damiao titanomagnetite ore deposit. North China Craton. Gondwana Res. 81, 240–251. https://doi.org/10.1016/j.gr.2019.12.001.

Wei, C.W., Xu, C., Chakhmouradian, A.R., Brenna, M., Kynicky, J., Song, W.L., 2020a. Carbon-strontium isotope decoupling in carbonatites from Caotan (Qinling, China): Implications for the origin of calcite carbonatite in orogenic settings. J. Petrol. 61, egaa024. https://doi.org/10.1093/petrology/egaa024.

Weidner, J.R., 1982. Iron-oxide magmas in the system Fe-C-O. Can. Mineral. 20, 555–566.

Willemse, J., 1969. The vanadiferous magnetic iron ore of the Bushveld Igneous Complex. Econ. Geol. 4, 187–208.

Wu, Y.B., Zheng, Y.F., Zhao, Z.F., Gong, B., Liu, X., Wu, F.Y., 2006. U-Pb, Hf and O isotope evidence for two episodes of fluid-assisted zircon growth in marble-hosted eclogites from the Dabie orogen. Geochim. Cosmochim. Acta 70, 3743–3761. https://doi.org/10.1016/j.gca.2006.05.011.

Xu, C., Taylor, R.N., Kynicky, J., Chakhmouradian, A.R., Song, W.L., Wang, L.J., 2011. The origin of enriched mantle beneath North China block: Evidence from young carbonatites. Lithos 127, 1–9. https://doi.org/10.1016/j.lithos.2011.07.021.

Yang, K., Fan, H., Pirajno, F., Li, X., 2019. The bayan Obo (China) giant REE accumulation conundrum elucidated by intense magmatic differentiation of carbonatite. Geology 47, 1198–1202. https://doi.org/10.1130/G46674.1.

Yavuz, F., 2021. Winmigob: A windows program for magnetite–ilmenite geothermometer and oxygen barometer. J. Geosci. 66, 51–70. https://doi.org/10.3190/jgeosci.319.

Zhang, R.X., Yang, S.Y., 2016. A mathematical model for determining carbon coating thickness and its application in electron probe microanalysis. Microsc. Microanal. 22, 1374–1380. https://doi.org/10.1017/S143192761601182X.

Zheng, H., Chen, H., Wu, C., Jiang, H., Gao, C., Kang, Q., Yang, C., Wang, D., Lai, C.K., 2020. Genesis of the supergiant Huayangchuan carbonatite-hosted uranium-polymetallic deposit in the Qinling Orogen, Central China. Gondwana Res. 86, 250–265. https://doi.org/10.1016/j.gr.2020.05.016.